AN OPTICAL SYSTEM TO TRANSFORM THE OUTPUT BEAM OF A QUANTUM CASCADE LASER TO BE UNIFORM

by

Jordan M. Jacobson

A thesis submitted in partial fulfillment
of the requirements for the degree

of

MASTER OF SCIENCE

in

Electrical Engineering

Approved:

Dr. Doran Baker Major Professor	Dr. Blake Crowther Committee Member
Dr. Jacob Gunther Committee Member	Dr. Mark R. McLellan Vice President for Research and Dean of the School of Graduate Studies

UTAH STATE UNIVERSITY
Logan, Utah

2016

Abstract

An Optical System to Transform the Output Beam of a Quantum Cascade Laser to be Uniform

by

Jordan M. Jacobson, Master of Science

Utah State University, 2016

Major Professor: Dr. Doran Baker
Department: Electrical and Computer Engineering

Quantum cascade lasers (QCLs) are a candidate for calibration sources in space-based remote sensing applications. However, the output beam from a QCL has some characteristics that are undesirable in a calibration source. The output beam from a QCL is polarized, both temporally and spatially coherent, and has a non-uniform bivariate Gaussian profile. These characteristics need to be mitigated before QCLs can be used as calibration sources. This study presents the design and implementation of an optical system that manipulates the output beam from a QCL so that it is spatially and angularly uniform with reduced coherence and polarization.

(85 pages)

Public Abstract

An Optical System to Transform the Output Beam of a Quantum Cascade Laser to be Uniform

by

Jordan M. Jacobson, Master of Science

Utah State University, 2016

Major Professor: Dr. Doran Baker
Department: Electrical and Computer Engineering

Quantum cascade lasers (QCLs) are a candidate for calibration sources in space-based remote sensing applications. However, the output beam from a QCL has some characteristics that are undesirable in a calibration source. These characteristics need to be mitigated before QCLs can be used as calibration sources. This study presents the design and implementation of an optical system that removes the undesirable characteristics from a QCL output beam, so it can be used as a calibration source.

Acknowledgments

Firstly, I would like to thank Dr. Doran Baker, Dr. Blake Crowther, and Dr. Jacob Gunther for the time they dedicated to give me guidance and advice to help me conduct this study. I would like to thank the Department of Energy for providing funding for this research under contract number DE-NA0001740. I would also like to thank the employees at the Space Dynamics Laboratory for the effort they contributed to this research, namely, Stewart Hansen, Alan Thurgood, Aaron Avery, Cory Harker, James Peterson, and Stephen Dansie. I would also like to thank Joe Kristl for helping with the data analysis for the output beam uniformity data, Bradley Balling for the providing the bidirectional reflection distribution function measurement data for Infragold, and those I corresponded with at Labsphere, namely Doug Baxter and Steve Weiss, for the information and services they provided.

Jordan M. Jacobson

Contents

List of Tables

List of Figures

Acronyms

SABER	Sounding of the atmosphere using a broadband emission radiometry
QCL	Quantum Cascade Laser
MWIR	Mid-wavelength Infrared
USU	Utah State University
FWHM	Full Width Half Maximum
FOV	Field of View
HFOV	Half Field of View
CPC	Compound Parabolic Concentrator
BRDF	Bidirectional Reflectance Distribution Function
SDL	Space Dynamics Laboratory
PNNL	Pacific Northwest National Laboratory
CAD	Computer-aided Design
CW	Continuous Wave
IR	Infrared

Chapter 1

Introduction

1.1 Motivation for Research

1.1.1 Space-Based Remote Sensing Calibration Sources

Calibration sources are a vital component in space-based remote sensing systems. Due in part to the challenging environment of space, detectors for remote sensing systems onboard a spacecraft change over time. Because of this change, the detectors need to be calibrated to ascertain their responsivities as a function of time. This calibration is generally accomplished by illuminating the detector with a known reference source and recording the detector system output as it responds to the known irradiance. These reference sources are the calibration sources for the remote sensing system.

Blackbody sources are commonly used as calibration sources because their output is a known function of temperature, which can be accurately measured, and the optical properties of their output are a good match to the optical properties of most natural scenes that will be viewed by the sensors being calibrated. An example of a remote sensing system that uses a blackbody as a calibration source for its sensor is the sounding of the atmosphere using a broadband emission radiometry (SABER) infrared radiometer [1]. Some of the disadvantages of blackbody sources are their mass, power consumption, size, and time required to warm up, stabilize, and change temperatures. The concept of using a quantum cascade laser (QCL) source for space-based calibration systems is based upon the premise that it could overcome most of the disadvantages of a blackbody source, and that it could enable new operating modes that cannot be achieved by a blackbody.

1.1.2 Quantum Cascade Laser as a Calibration Source

The QCL was invented in 1994 at Bell Laboratories [2]. It is a semiconductor laser that operates primarily in the mid-wavelength infrared (MWIR) range [3]. The active region of a QCL is made up of a sequence of two alternating layers of semiconductor materials, known as a superlattice [2]. The heterostructure created by the alternating semiconductor materials forms a series of quantum wells [3]. This quantum-mechanical structure enables electronic transitions of electrons between states that belong to the same energy band. These transitions are known as intersubband transitions, and are fundamentally different from the interband transitions that occur in semiconductor diode lasers [2, 3]. The wavelength of the light emitted from a laser is proportional to the transition energy in the semiconductor material [4]. The transition energy of an intersubband transition is the difference between the confinement energies of the electronic states [3]. These confinement energies can be tuned by changing the quantum well width, or in other words, by changing the thickness of the semiconductor layers in the superlattice [3]. The ability to adjust the transition energy by changing the thickness of the semiconductor layers allows QCLs to emit light over a very large wavelength range [2, 3, 5, 6]. A great deal of research has been focused on the quantum engineering of QCLs to operate at many different wavelengths. QCLs have been demonstrated to operate between the wavelengths of 3 – 16 μm at room temperature and 60 – 250 μm at cryogenic temperatures [3].

The QCLs used for this project have a center wavelength of about 4.55 μm. QCLs are small devices with low power consumption, which make them a desirable candidate for a calibration source. The active region of a QCL is on the order of tens of micrometers across [3]. The QCLs used for this design are mounted on a C-mount package that has the dimensions 6.4 mm x 4.3 mm x 7.9 mm. These QCLs have an optical output power of approximately 450 mW, and an operating current of approximately 900 mA [7]. One characteristic of QCLs that makes them desirable as a calibration source is their fast turn-on time. Unlike a blackbody, QCLs can turn on and stabilize within a few milliseconds if the thermal control system can respond and stabilize the temperature that quickly. As a

practical matter, most QCLs can stabilize within a 10 to 20 second time period.

It is important to note that a QCL source would only be able to replace a blackbody source in some specific remote sensing applications. In some applications the modalities enabled by the ability to tune the QCL emission to a wavelength beyond the spectral range of a blackbody is desired. In other applications the broadband spectral radiance of a blackbody source is more desirable than the single-band spectral radiance of a QCL source. In many cases it would be beneficial to include both a QCL-based calibration source and a blackbody-based calibration source in the remote sensing system to broaden the potential applications of the system.

QCLs have some undesirable characteristics that would need to be overcome before they would be a good candidate for a calibration source. The output from a blackbody is uniform and can be modified by optics or baffling to emit from a solid angle that matches the F-number of the instrument being calibrated. In contrast, a QCL output beam has a highly non-uniform bivariate Gaussian profile which would need to be homogenized by an optical system before it could be used as a calibration source. In addition, the output beam from the QCL is polarized to some degree, and the output beam is both temporally and spatially coherent. The partially polarized light could cause calibration inaccuracies because it could transmit through the system differently than unpolarized light from a natural scene. The coherence of the QCL output beam could cause speckle on the image plane due to the beam interfering with itself. This will cause a non-uniform irradiance pattern on the sensor which could cause noise in the system, or readings of false irradiance levels. For a QCL-based calibration system to be successful, the output beam from the QCL will have to be manipulated by an optical system so that it is a uniform beam with reduced coherence and polarization.

1.1.3 Overview of Quantum Cascade Laser Calibration Source Project

Utah State University (USU) is leading a project that has a primary objective to produce a QCL-based calibration source system that can be used for space-based instrument calibration. The QCL calibration source system being developed is made up of five main

subsystems. Each of these subsystems is represented by a block in the functional block diagram shown in Fig. 1.1. The first four blocks in the diagram were designed and implemented prior to the work which is presented in this thesis. The precision current controller for the QCL was designed and fabricated at USU by Hansen [8]. The temperature controller, QCL, and the appropriate QCL mount are all commercial parts. The driving software for each hardware module has been developed, and was used to test the integrated precision current controller, temperature controller, and QCL to ensure that they all perform together correctly. The research presented in this thesis is based upon the design and implementation of the optical system that is represented by block 5 in the block diagram of Fig. 1.1.

1.2 Objectives of Thesis Research

The three main objectives of the research presented in this paper are listed below:

1. Create a design for an optical system that manipulates the output beam from a QCL so that it is spatially and angularly uniform with reduced coherence and polarization.

2. Implement the optical system in hardware with the rest of the calibration source system modules, and test its functionality.

3. Analyze the data from the hardware tests to determine if the constructed QCL calibration source would be a good candidate as a space-based remote sensing calibration source.

1.3 Thesis Outline

The remainder of this paper is structured as follows: In Chapter 2 the initial optical model design is presented. An outline of the optical model design process is described in detail in Chapter 3. Chapter 4 gives a summary of the testing plan for the hardware tests. The data processing and analysis techniques used to process the data collected from the hardware tests are described in Chapter 5. A comparison of the simulation results and the hardware test results is given in Chapter 6. Finally, the main conclusions gathered from the project are stated in Chapter 7.

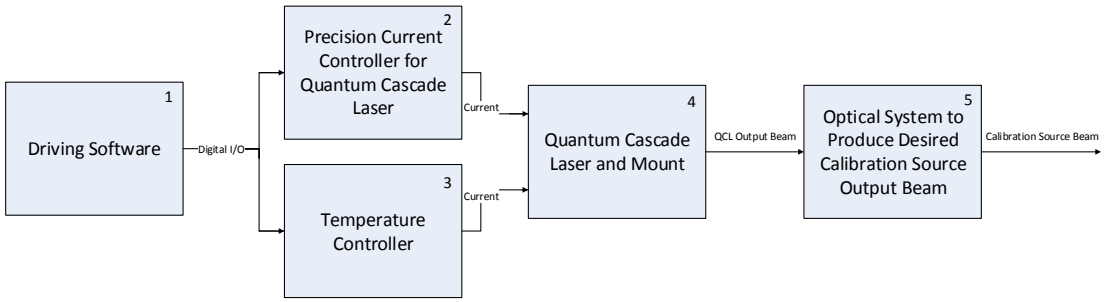

Fig. 1.1: Quantum Cascade Laser Calibration Source System Block Diagram.

Chapter 2

Initial Optical Model Design

2.1 Initial Optical System Concept

The initial design concept for the optical system is shown in Fig. 2.1. This concept consists a QCL source, a conically baffled integrating sphere, and a plano-convex lens [9]. The conically baffled integrating sphere accepts a portion of the output beam from the QCL. The beam that enters the integrating sphere is homogenized by undergoing multiple diffuse reflections off the inner surfaces of the sphere. The homogenized output beam from the integrating sphere is captured by a lens that will create a beam with the desired solid angle of the output beam of the system. An optical model of each of the components shown in the figure was generated, so that an overall optical model for the initial design concept could be created.

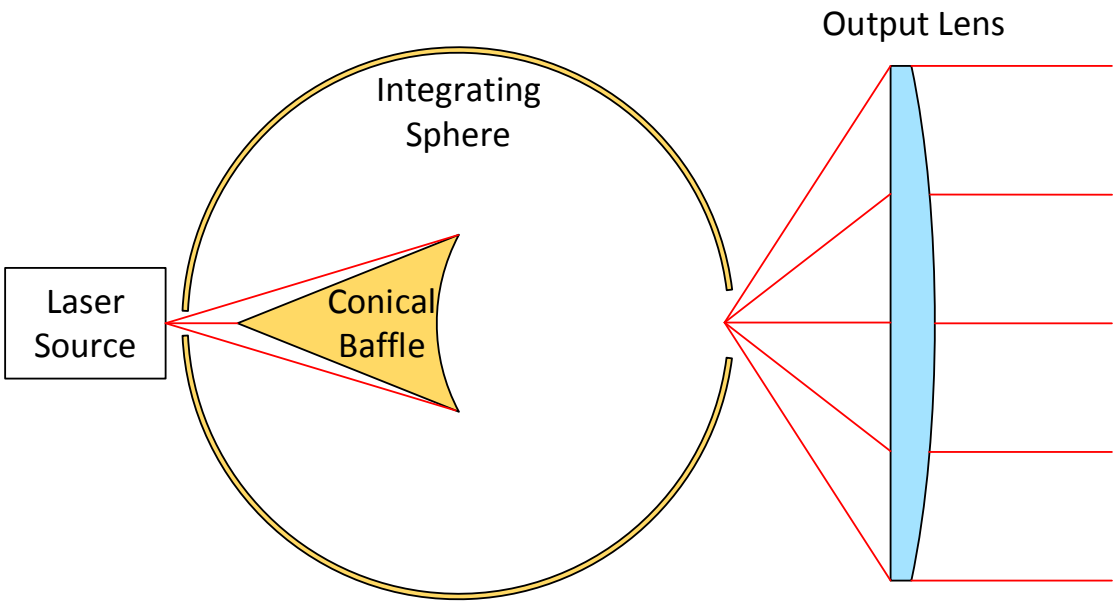

Fig. 2.1: The initial design concept for the optical system.

2.1.1 Quantum Cascade Laser Source Optical Model

An optical model for a QCL source was developed using the manufacturer specifications for the QCL output beam profile. The manufacturer provides full width half maximum (FWHM) beam divergence angles for the directions parallel and perpendicular to the active region of the QCL. The parallel FWHM beam divergence is 30°, and the perpendicular FWHM beam divergence is 50° [7]. This creates an elliptical beam that has an intensity profile that can be described by the bivariate Gaussian equation shown in Equation (2.1), where I is the intensity of the output beam, I_0 is the intensity at the optical axis or center of the propagating field, C_x and C_y are constants, and l and m are direction cosines in the x and y directions, respectively. The constants C_x and C_y can be solved for using the QCL beam divergence geometry shown in Fig. 2.2, to give the expressions for the constants shown in Equations (2.2) and (2.3). Combing Equations (2.1) – (2.3) an expression for the intensity of the output beam from the QCL is obtained, which is shown in Equation (2.4). This expression was used to create an optical model for the QCL source.

$$I(l,m) = I_0 e^{-C_x l^2 - C_y m^2} \tag{2.1}$$

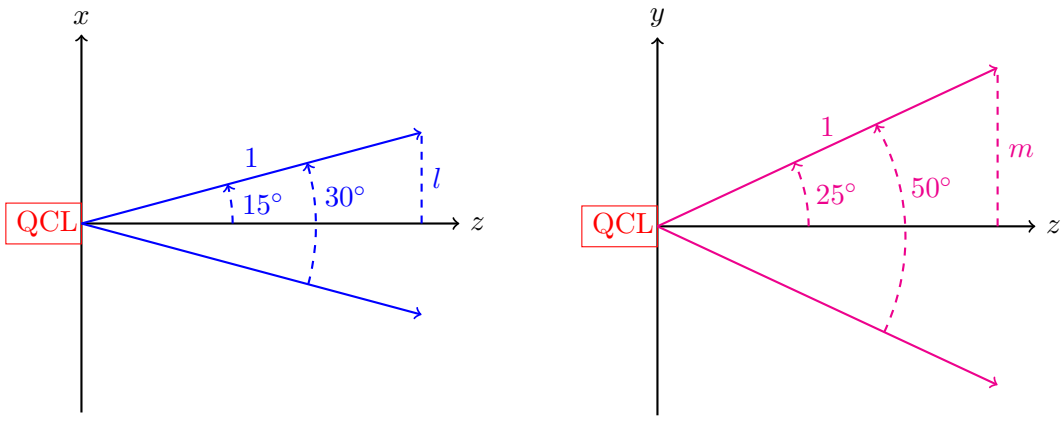

(a) QCL horizontal beam divergence.

(b) QCL vertical beam divergence

Fig. 2.2: Plots of beam divergence angles.

$$C_x = \frac{ln(2)}{sin^2(15°)} \tag{2.2}$$

$$C_y = \frac{ln(2)}{sin^2(25°)} \tag{2.3}$$

$$I = I_0 e^{-\left[\frac{ln(2)}{sin^2(15°)}l^2 + \frac{ln(2)}{sin^2(25°)}m^2\right]} \tag{2.4}$$

The output power for the QCL source model was set to 1 W for ease of efficiency calculations. The actual output power from the QCLs being used is around 450 mW. Figure 2.3 shows intensity plots from the simulation of the QCL source model. As can be seen in Figure 2.3b and Figure 2.3c, the model is a good representation of a QCL source based on the FWHM parameters from the manufacturer.

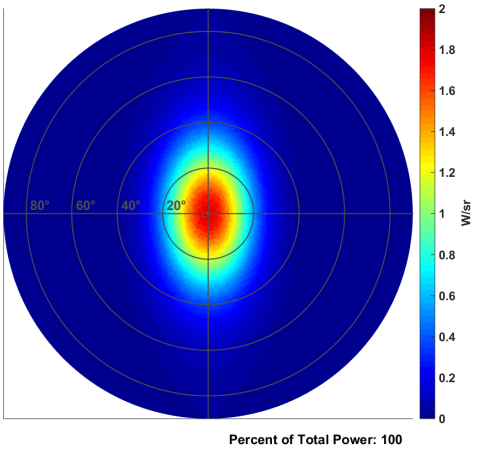

(a) QCL intensity profile.

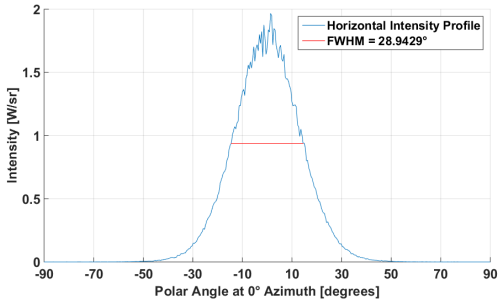

(b) QCL intensity profile at 0° azimuth.

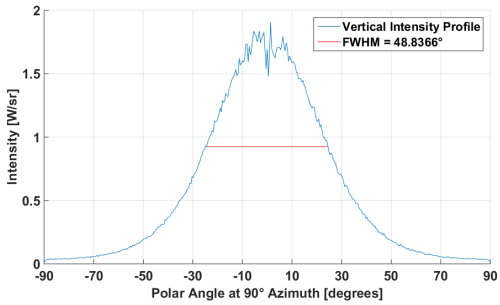

(c) QCL intensity profile at 90° azimuth.

Fig. 2.3: Simulation results of QCL source model.

2.1.2 Conically Baffled Integrating Sphere Design

The sphere designed for this project has an output port located 180° from the input port with a conical baffle mounted in the center of the sphere to block the direct path between the two ports. The conically baffled integrating sphere was selected in order to increase the efficiency of the system. The conical baffle mounted in the center of the sphere is oriented to direct the light towards the output port of the sphere.

In the initial optical model, the integrating sphere was 25.4 mm in diameter with an input port diameter of 3 mm and an output port diameter of 6 mm. The dimensions for the integrating sphere design are proportional to the dimensions of a similar design for a conically baffled integrating sphere designed by Crowther [9]. In order for an integrating sphere to work properly, the inner surfaces of the sphere need to be coated with a diffuse coating [10]. As light traverses the sphere, it undergoes many diffuse reflections which homogenize the beam. Because QCLs operate in the MWIR range, the inner surfaces of the sphere were modeled as diffuse reflectors, either Lambertian reflectors or Infragold, a common diffusely reflecting material produced by Labsphere, Inc. [11]. At the beginning of the design process, it was assumed that the surfaces inside the sphere were Lambertian with a reflectance of 95%, which is the reflectance of Infragold for the wavelength of the QCLs being used [11].

The initial dimensions for the conical baffle were also based on the design by Crowther [9]. The base of the conical baffle was designed to be spherical with the curvature centered on the output port of the integrating sphere. In the model, the conical baffle was positioned with the vertex of the spherical base located at the center of the integrating sphere. Figure 2.4 shows the initial dimensions of the integrating sphere and conical baffle. The base width of the conical baffle was iteratively changed at multiple stages of the design process in order to determine the best configuration. These changes and other aspects of the iterative design process will be discussed later in this thesis.

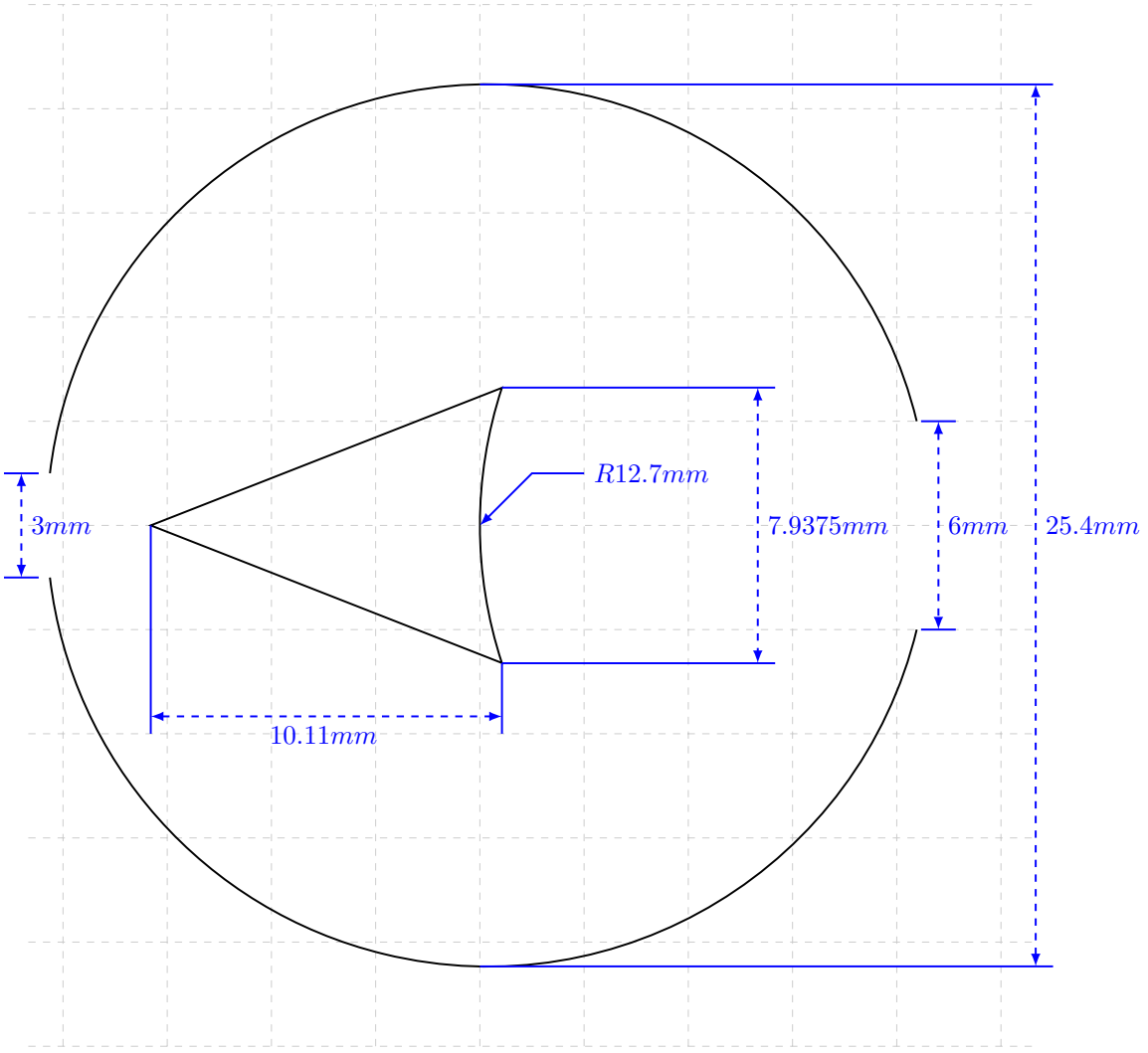

Fig. 2.4: Initial dimensions of integrating sphere and conical baffle

2.1.3 Output Lens Design

It was desired for the lens to be F/1 in order to capture as much light as possible. The field of view (FOV) was set to 15°, with a goal of using the central 10°. An initial estimate of the focal length of the lens was calculated using these constraints along with the diameter of the output port of the sphere. Figure 2.5 is a simple drawing of the integrating sphere output port and the lens. The variables D and SD in Fig. 2.5 represent the diameter and semi-diameter of the output aperture of the integrating sphere. The lens FOV and half field of view (HFOV) parameters are represented by the variables FOV and $HFOV$, respectively.

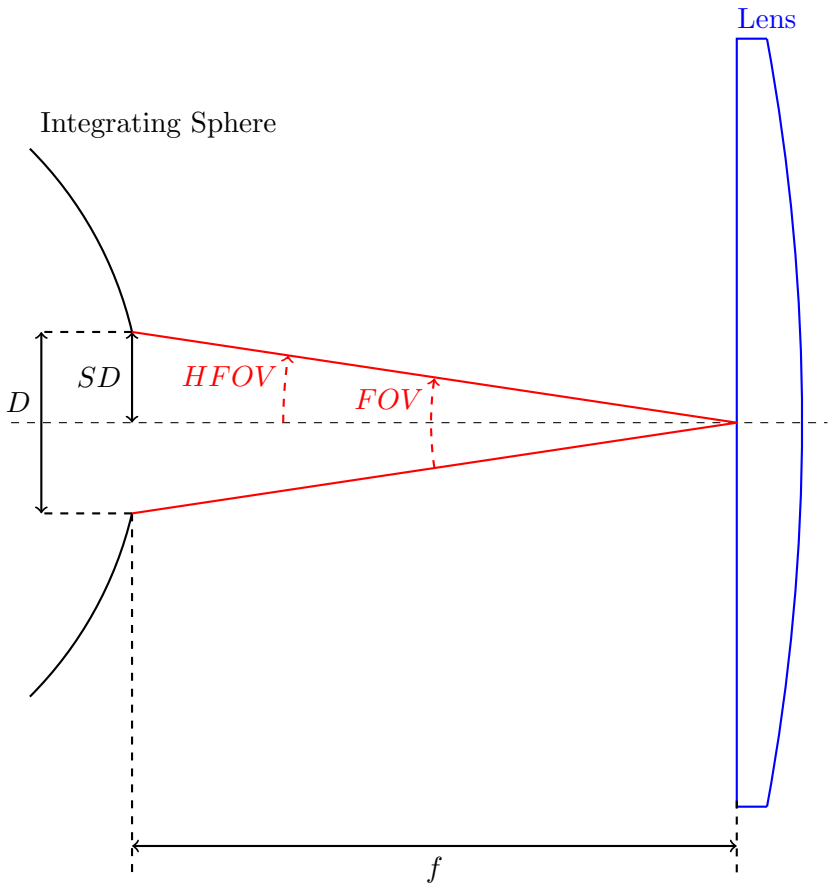

Fig. 2.5: Lens Design Drawing

Equation (2.5) for the focal length of the lens was generated using the geometry from Fig. 2.5. Using this equation an initial focal length of 22.79 mm was calculated.

$$f = \frac{SD}{tan(HFOV)} \tag{2.5}$$

This initial estimate for the focal length was used to find a commercial off the shelf lens that would work with the system. There are many 25-mm commercial lenses available. The lens selected for this project was a silicon plano-convex lens because it was inexpensive and fit within the budget constraints of the project. Once a commercial lens was selected, the distance between the output aperture of the integrating sphere and the lens was optimized. The optimized distance was determined to be 22.37 mm. This distance was used in the optical model in order to position the lens with respect to the integrating sphere.

2.2 Standard Simulation Environment Configuration

A standard simulation configuration was established in order to facilitate comparison of simulation results between optical models. Twenty million rays were traced for every simulation. The power contained in the twenty million rays for each simulation was fixed at 1 W.

The detectors in all of the simulation models have the same number of pixels. Detectors or receivers were placed at the same three locations for every simulation. The first detector was placed at the input port to the system. For the initial design, this location is at the input port of the integrating sphere. This location provides information about the beam entering the optical system and any energy lost from light radiating out of the input port of the system. The second detector was placed at the output aperture of the integrating sphere. This location provides information about the uniformity of the beam as it exits the sphere. The third detector was placed at the output of the lens, which is also the system output. This is the primary location of interest because a portion the output beam from the lens is the calibration source beam. The central 10 mm of the lens output beam is the portion that was set as the region of interest for calibration. This 10-mm diameter beam is identified by a circle on all of the lens output irradiance simulation plots. Figure 2.6 shows the detector locations with respect to the initial design. Irradiance is the measure of incident power per unit area, and intensity is the measure of power per solid angle. At each detector location, both the irradiance and intensity were simulated. Each set of simulation results presented in this work contain irradiance or intensity data from one or more of these locations.

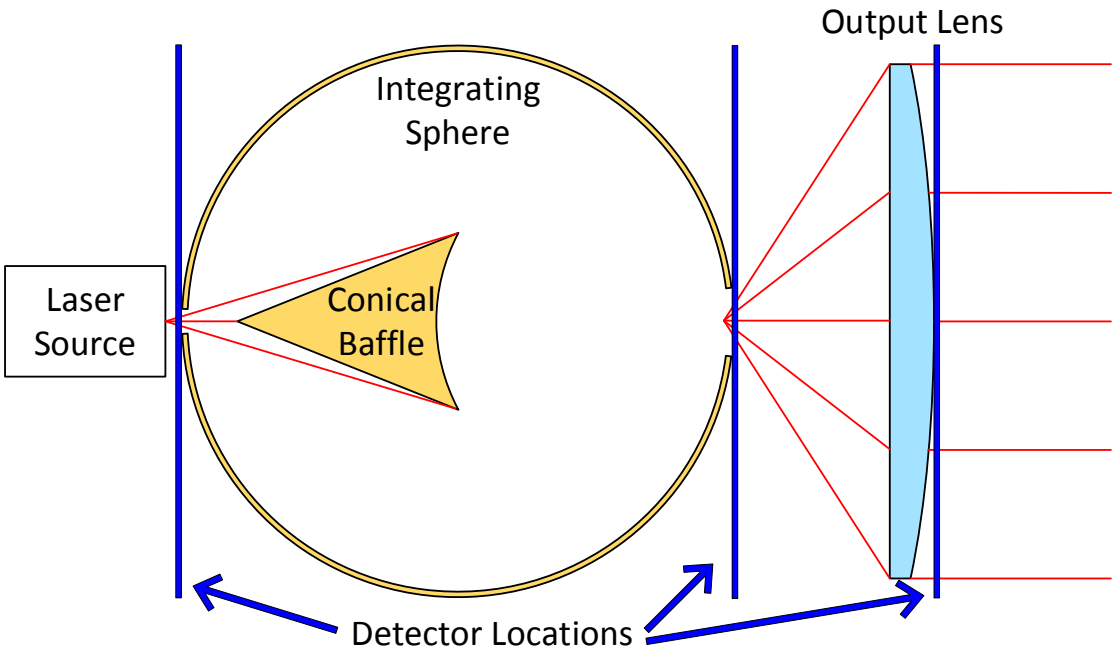

Fig. 2.6: Diagram Showing the Locations of the Simulation Detectors

2.3 Simulation of Initial Design Concept

The initial design was simulated as described above. Figure 2.7 shows irradiance plots at the sphere input port to characterize both the light entering the system, and the light being lost out the input port. Figure 2.8 shows irradiance and intensity plots at the sphere output port to characterize the light exiting the sphere. Figure 2.9 shows irradiance and intensity plots at the lens output that illustrate the nature of the system output beam.

The system output is quite uniform across the 10-mm diameter beam of interest in the lens output irradiance plot shown in Fig. 2.9a and the 5° HFOV of interest in the lens output intensity plot shown in Fig. 2.9b. However, a few issues can be seen in the plots at the other two locations. In Fig. 2.8a, an obvious bright spot can be seen in the center of the irradiance measured at the output of the integrating sphere. Ideally, the output beam from the integrating sphere should be nearly Lambertian, so this bright spot is undesirable.

Another undesirable characteristic of this system is the amount of energy that is lost exiting the system out the integrating sphere input port. In Fig. 2.7b, it can be seen that

more than 7% of the total optical power input into the system is lost out the integrating sphere input port. This is more than twice the amount of power that reaches the detector at the output of the system. This result caused this design to be refined because of the danger that damage might be done to the QCL by optical power being reflected back into the laser.

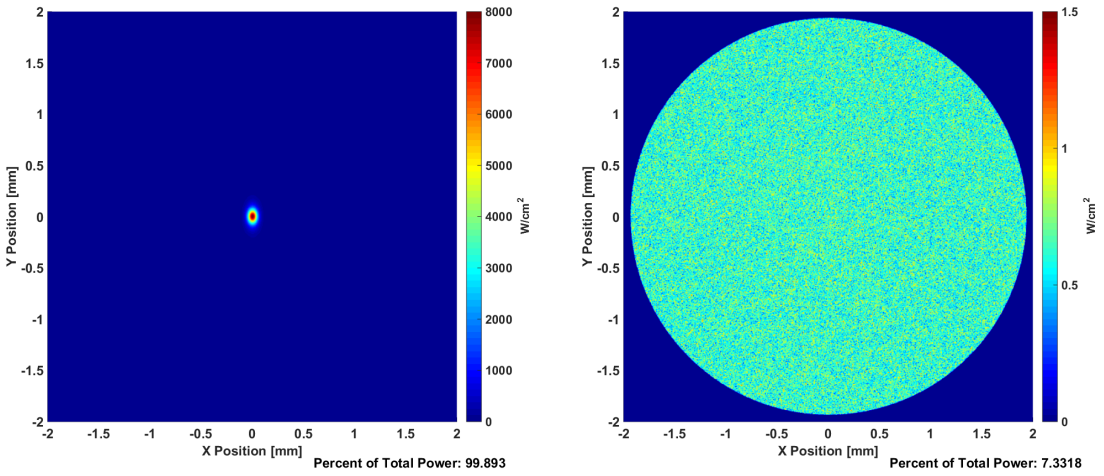

(a) Initial Design: Sphere Input Irradiance (b) Initial Design: Energy Lost out Input Port

Fig. 2.7: Initial Design Sphere Input Detector Plots

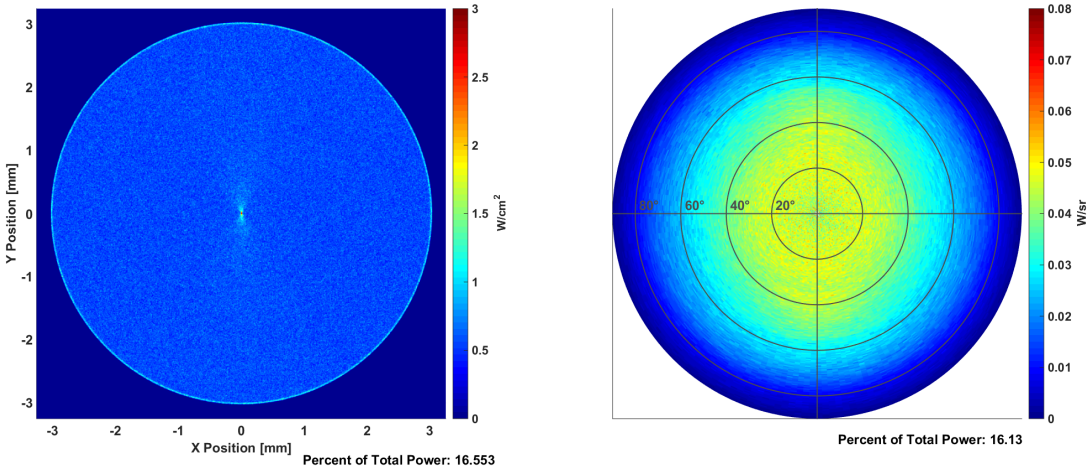

(a) Initial Design: Sphere Output Irradiance (b) Initial Design: Sphere Output Intensity

Fig. 2.8: Initial Design Sphere Output Detector Plots

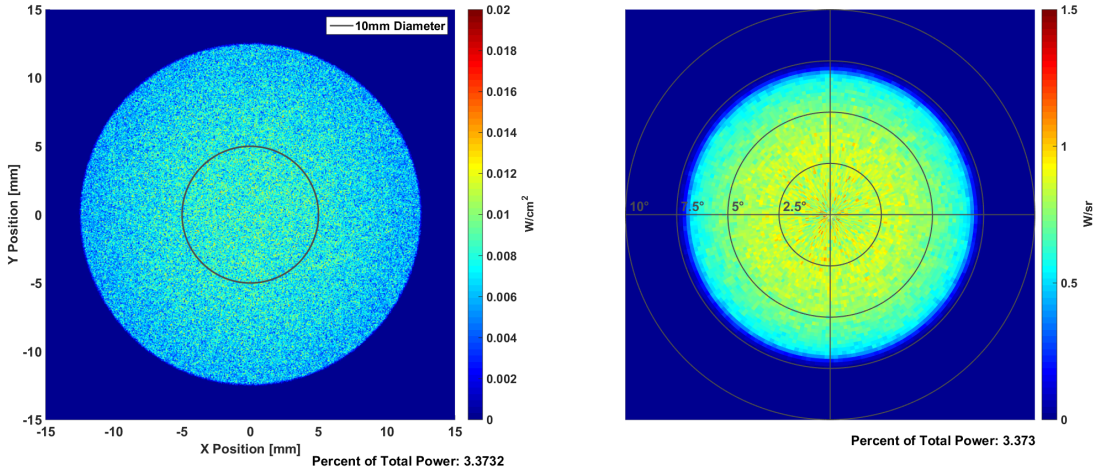

(a) Initial Design: Lens Output Irradiance (b) Initial Design: Lens Output Intensity

Fig. 2.9: Initial Design Lens Output Detector Plots

A few iterations of modifications were made to the initial design in order to mitigate the issues described above. The next chapter describes the design iteration process followed in order to reduce the number of undesirable characteristics from the source system optical model.

Chapter 3

Optical Model Design Iterations Based on Simulation Results

3.1 Compound Parabolic Concentrator

The simulation results for the initial design had some undesirable characteristics that were mentioned in the previous chapter. The first of these undesirable characteristics is the non-uniform irradiance pattern at the output of the integrating sphere. Figure 2.8a shows this irradiance pattern, which exhibits an obvious bright spot in the center. By analyzing the path analysis data from the ray trace, it was ascertained that this bright spot was due to the high divergence angles from the output of the QCL. These high divergence angles generated rays that traversed the integrating sphere with a single reflection. These rays exited the QCL at angles so large that they were not suppressed by the conical baffle, but instead hit the side wall of the integrating sphere once, and then bounced through the output aperture of the integrating sphere. This is an undesirable characteristic of the system because it generates a non-uniform irradiance pattern at the output from the integrating sphere.

To remove this bright spot from the irradiance pattern detected at the output of the integrating sphere, an inverted compound parabolic concentrator (CPC) was added to the design between the QCL and the input to the integrating sphere. A basic layout showing the addition of the CPC is shown in Fig. 3.1. The CPC was designed to reduce the divergence of the beam from the QCL so that the entire beam would strike the conical baffle before hitting any other surface in the sphere. Figure 3.2 shows the geometry of the CPC. The CPC was designed to have the desired maximum divergence angle using Equation (3.1), where a is the semi-diameter of the input aperture, L is the length of the CPC, and θ_{max} is the maximum divergence angle of the beam exiting the CPC [12].

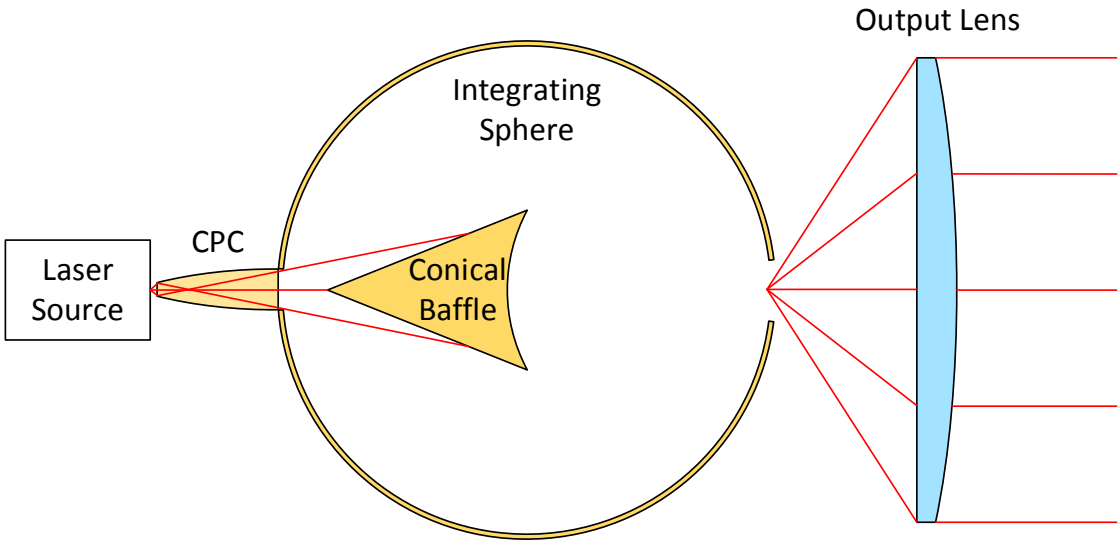

Fig. 3.1: Diagram showing the addition of the CPC.

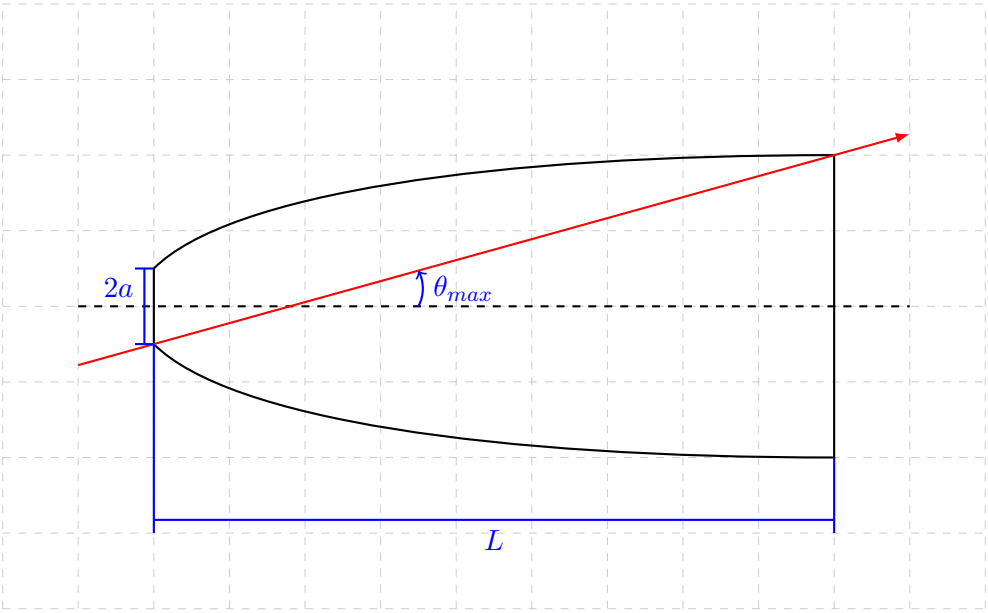

Fig. 3.2: CPC geometry.

$$L = \frac{a(1 + sin(\theta_{max}))}{tan(\theta_{max})sin(\theta_{max})} \tag{3.1}$$

Some of the initial simulation results of the optical model with the CPC added are shown in Fig. 3.3. An improvement in the uniformity of the irradiance pattern at the

output of the integrating sphere can be seen in the 3.3. The conical baffle base width was iteratively changed at this stage of the design to determine the baffle size that would work best for the integrating sphere diameter of 25.4 mm. Through this iterative process, it became apparent that the irradiance pattern at the output of the integrating sphere was still non-uniform for most of the different conical baffle sizes. An example of this is shown in Fig. 3.4 when the conical baffle had a base width of 11.94 mm.

It was determined that the cause of the non-uniform irradiance pattern at the output of the integrating sphere was due to the extreme irradiance non-uniformity in the beam exiting the CPC and entering the integrating sphere. Even though the CPC decreased the divergence angles of the beam exiting the QCL, it has a highly non-uniform output beam. The irradiance entering the integrating sphere is shown in Fig. 3.5. This figure illustrates that there are two small areas on the vertical axis where the irradiance of the beam entering the sphere is larger than the rest of the area of the input port. Having so much of the irradiance focused on these two small areas created some common ray paths through the sphere which caused a non-uniform distribution of irradiance on the detector at the output of the sphere.

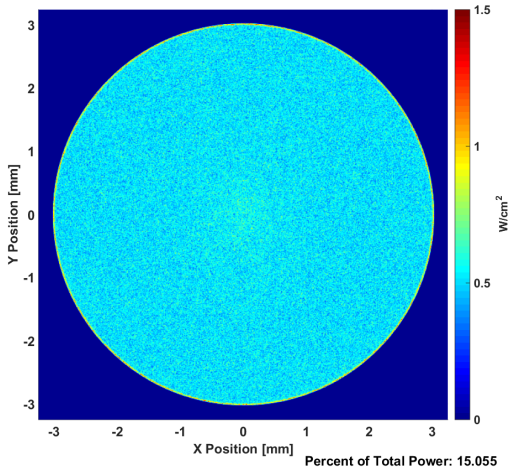

Fig. 3.3: Irradiance at the output of the integrating sphere with a CPC included in the optical model. The conical baffle base width is 7.94 mm for this case.

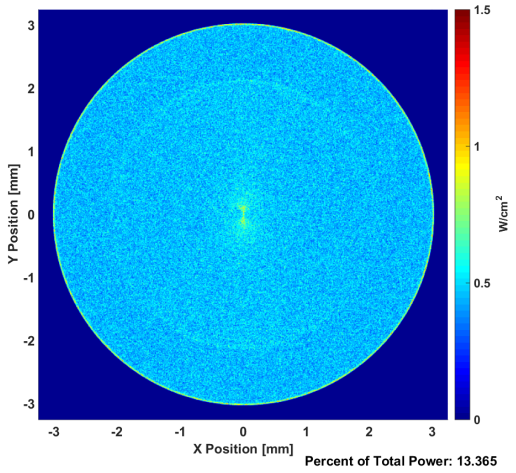

Fig. 3.4: Irradiance at the output of the integrating sphere with a CPC included in the optical model. The conical baffle base width is 11.94 mm for this case. The irradiance pattern is non-uniform.

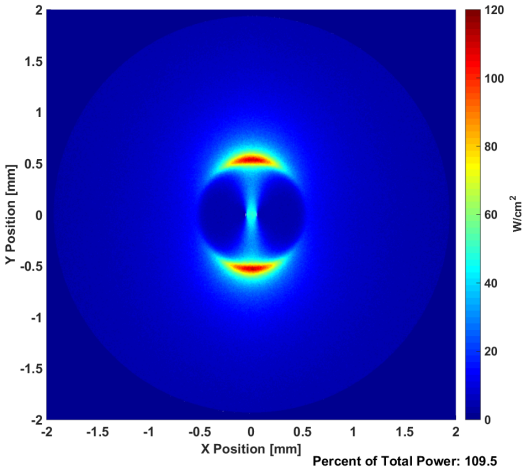

Fig. 3.5: Irradiance at the input to the integrating sphere with a CPC included in the optical model.

3.2 Conical Light Pipe

The CPC in the design was replaced with a conical light pipe in an attempt to make the beam being input into the integrating sphere more spatially uniform. Figure 3.6 shows a diagram of the optical model with the conical light pipe instead of the CPC at the input to the integrating sphere. The input port diameter, output port diameter, and length of the

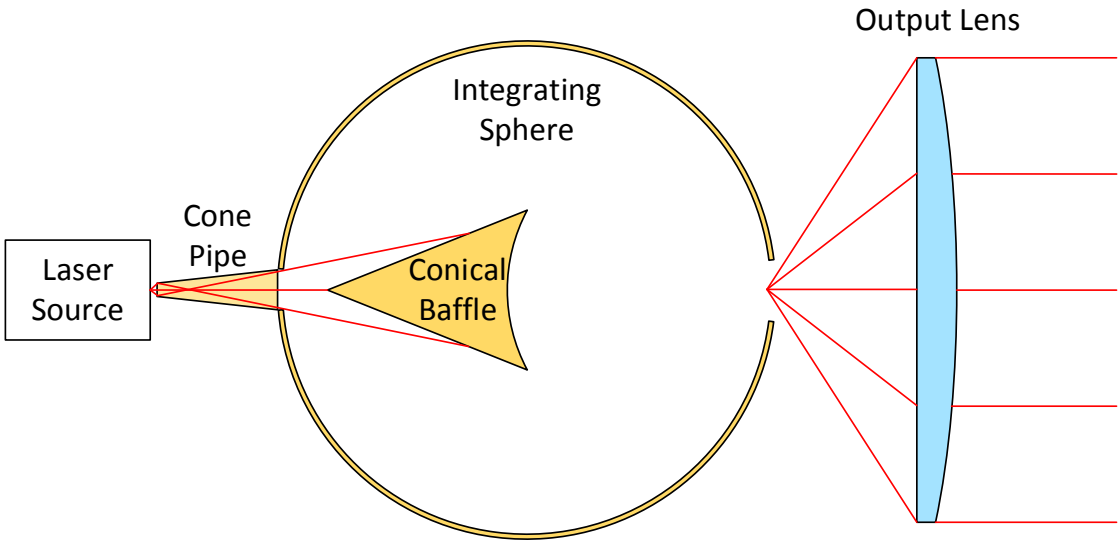

Fig. 3.6: Diagram of the optical model with a conical light pipe at the input to the integrating sphere.

conical light pipe are the same as the dimensions calculated for the CPC. The calculation of the divergence angle is the same for both components.

The simulation results for this model show that the irradiance at the input port of the integrating sphere is similar to the irradiance with just the QCL at the input to the sphere. However, having the conical light pipe between the QCL and the integrating sphere decreases the divergence of the beam so that rays cannot traverse the sphere with only one reflection. The irradiance at the input port to the integrating sphere is shown in Fig. 3.7. Figure 3.8 shows the detector plots at the output of the integrating sphere, and Fig. 3.9 shows the detector plots at the output of the lens. The spatial uniformity of the beam at the output to the integrating sphere was significantly improved by replacing the CPC with a conical light pipe. The irradiance at the output of the lens is also uniform across the beam.

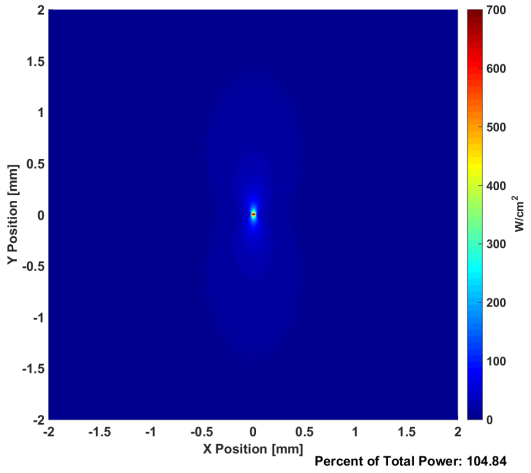

Fig. 3.7: Irradiance at the input port to the integrating sphere with a conical light pipe between the QCL and the integrating sphere.

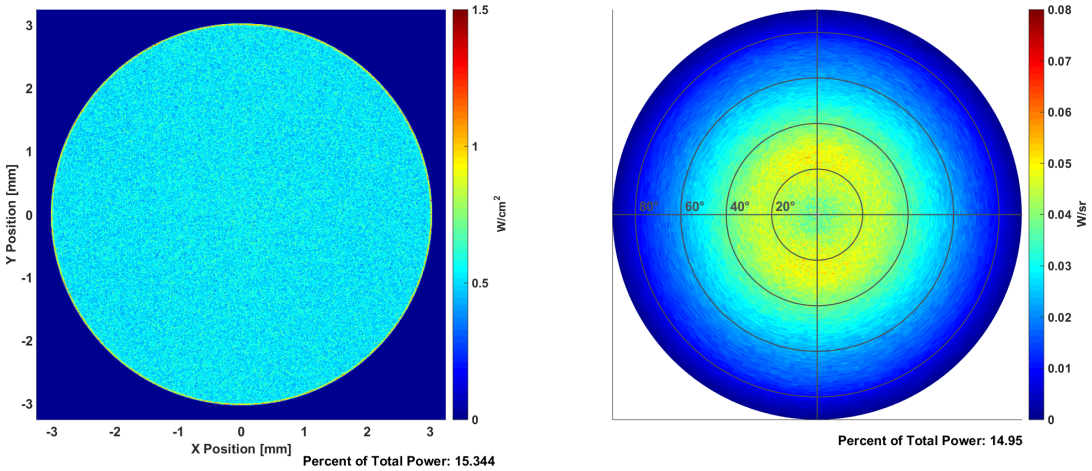

(a) Integrating sphere output irradiance.

(b) Integrating sphere output intensity.

Fig. 3.8: Detector images at the output of the integrating sphere with conical light pipe at the input port to the integrating sphere.

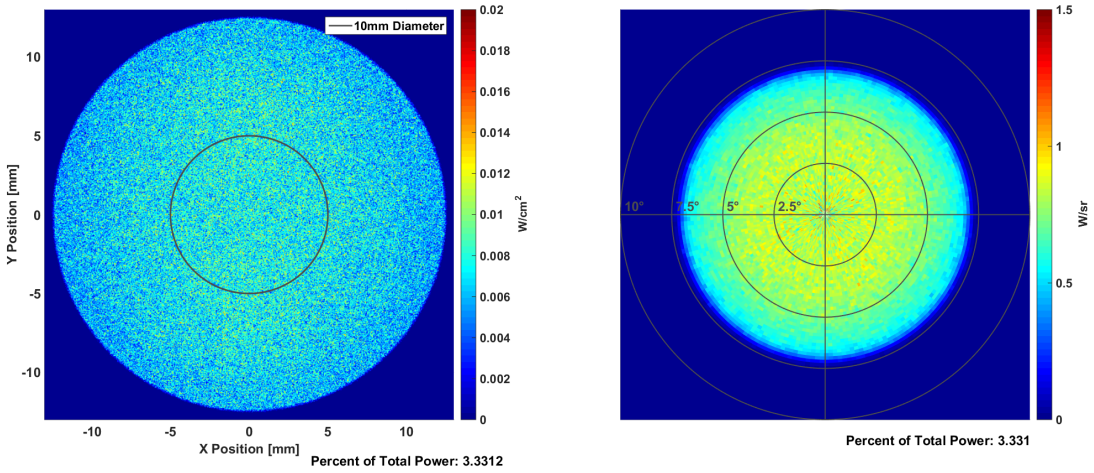

(a) Lens output irradiance.

(b) Lens output intensity.

Fig. 3.9: Detector images at the output of the lens with conical light pipe at the input port to the integrating sphere.

3.3 Infragold Bidirectional Reflection Distribution Function Model

The components of the optical system were selected and simulated in the optical model to show that they produce an output beam with the desired characteristics. However, the fidelity of the model needed to increase in order to make the optical model more accurate. For an integrating sphere to work properly, the reflections of light off the inner surfaces should be as Lambertian as possible. The simulations discussed in this paper so far assumed the inner surfaces of the integrating sphere were ideal Lambertian surfaces. No surface is ideally Lambertian, so the Bidirectional Reflection Distribution Function (BRDF) of the surfaces inside the sphere needed to be added to the optical model.

The BRDF of a surface is given by the function $f_r(\theta_i, \phi_i; \theta_r, \phi_r)$ which is defined by Equation (3.2), where θ_i and ϕ_i are respectively the polar and azimuth angles of the incident beam, θ_r and ϕ_r are respectively the polar and azimuth angles for the reflected beam, E_i is the incident irradiance, and L_r is the reflected radiance [13]. Given a beam incident on a surface, the BRDF equation physically represents the ratio of the radiance reflected from the surface to the irradiance incident on the surface, and it has units of sr^{-1}. Figure 3.10 shows a coordinate system that visually depicts the parameters of the BRDF of a surface.

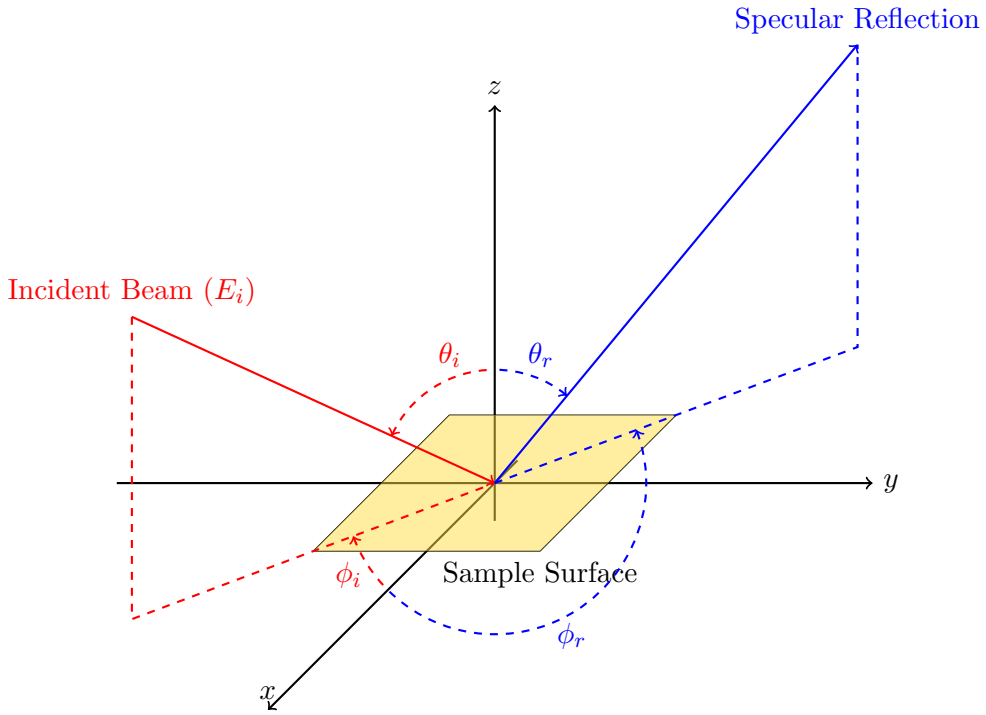

Fig. 3.10: BRDF coordinate system.

$$f_r(\theta_i, \phi_i; \theta_r, \phi_r) = \frac{dL_r(\theta_r, \phi_r)}{dE_i(\theta_i, \phi_i)} \tag{3.2}$$

Infragold, a special diffuse reflective surface coating from Labsphere, is a commonly used diffuse reflector in the MWIR range, and was the surface preparation planned for the reflective components of the source system. However, time and budget constraints did not allow the measurement of the Infragold BRDF data as part of this project. A BRDF data set containing both in-plane and out-of-plane measurements was desired so that the most accurate model of the Infragold could be added to the surfaces in the optical model. The problem was, no out-of-plane BRDF data could be found. A few sources were found that had collected in-plane BRDF data for Infragold, but none had collected out-of-plane data. The data used for the BRDF model generated for this project was provided by Balling who collected the data as part of his Masters Thesis Research [14]. An Infragold BRDF model was created by linearly interpolating the in-plane data around the azimuth angles to generate a full BRDF representation. Linear interpolation is performed by generating a line

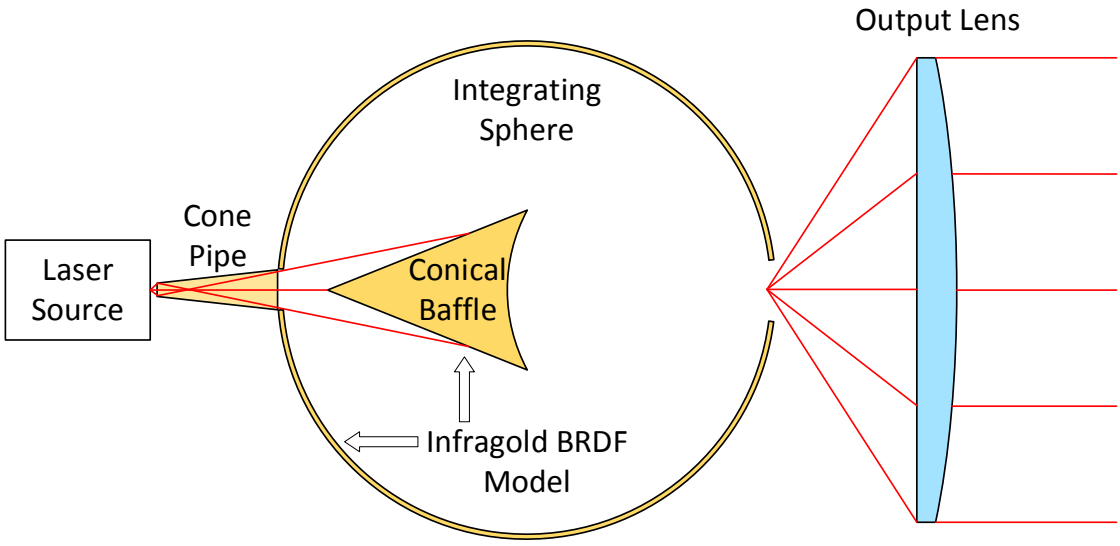

Fig. 3.11: Diagram indicating the surfaces to which the Infragold BRDF model was applied.

between two data points, and then inserting one or more additional data points at desired intervals along that line. This Infragold BRDF model was applied to the inner surface of the integrating sphere and to the surfaces on the conical baffle in the optical model as indicated in the diagram shown in Fig. 3.11.

As shown in the simulation results in Fig. 3.12 – Fig. 3.14, the output from the system is still uniform with the Infragold BRDF model applied. The two noticeable differences with the Infragold BRDF model applied are first, the reduction in power lost out the input port of the integrating sphere, and second, the increased concentration intensity of the beam on the vertical axis as it exits the integrating sphere. Both of these differences are due to Infragold having a specular component that directs more of the energy in the forward scatter direction compared to a Lambertian reflector.

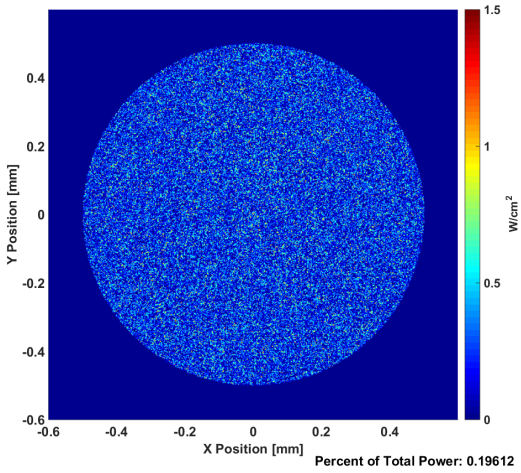

Fig. 3.12: Irradiance at the input port to the integrating sphere with Infragold BRDF model added to the integrating sphere and conical baffle surfaces.

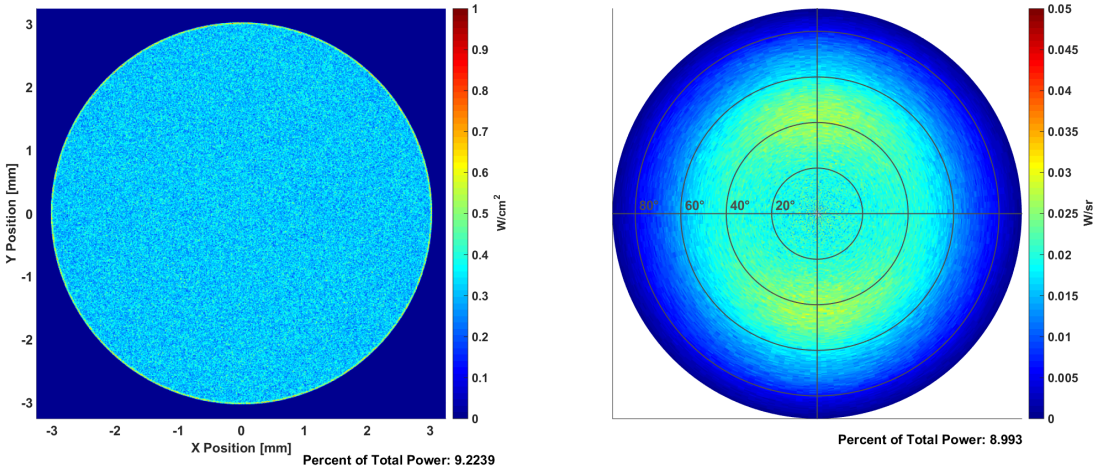

(a) Integrating sphere output irradiance.

(b) Integrating sphere output intensity.

Fig. 3.13: Detector images at the output of the sphere with Infragold BRDF model added to the integrating sphere and conical baffle surfaces.

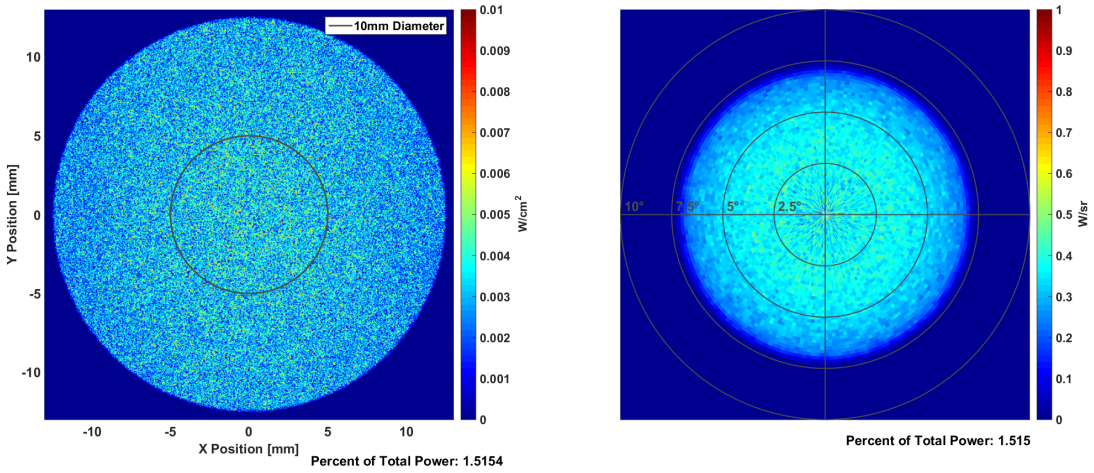

(a) Lens output irradiance.

(b) Lens output intensity.

Fig. 3.14: Detector images at the output of the lens with Infragold BRDF model added to the integrating sphere and conical baffle surfaces.

3.4 Model of Spider Support Vanes

As the drawings for the hardware implementation of the optical system were being developed, a method for supporting the conical baffle within the integrating sphere was created. This method consisted of three spider vanes that protrude out of the conical baffle and connect to the wall of the integrating sphere. The distance between the QCL and the input port to the conical light pipe was also modeled. A separation distance of 0.5 mm was inserted between the QCL and the input port to the conical light pipe. This was done to avoid damaging the QCL by contacting the facet of the laser. A diagram showing these two configuration changes is displayed in Fig. 3.15.

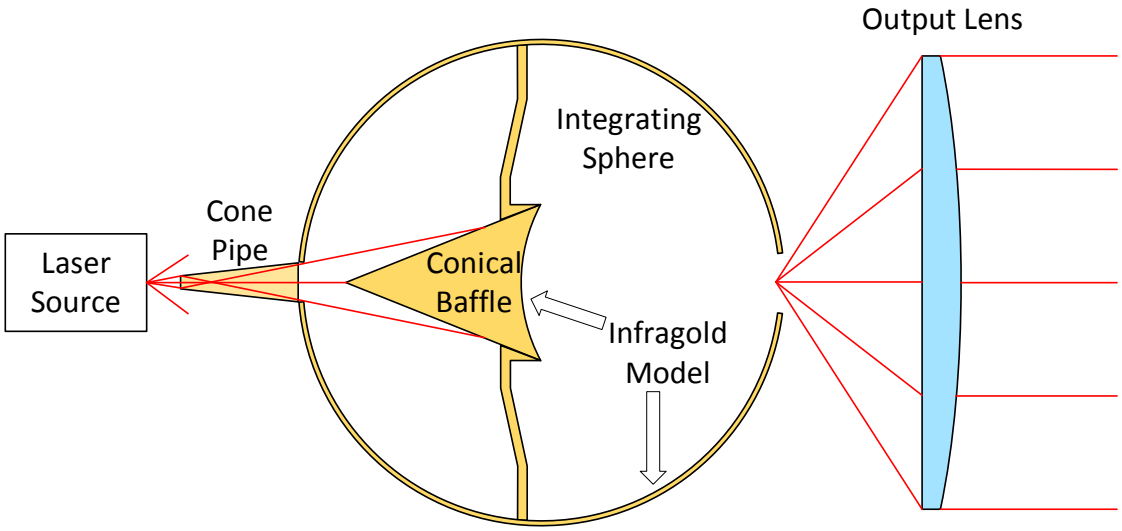

Fig. 3.15: Diagram showing the spider support vanes, and separation between the QCL and the conical light pipe.

This enhanced representation of a real design was simulated. The only significant differences between the results of this configuration and the previous case were a small decrease in energy reaching the output port, and a decrease in the intensity profile at the output of the integrating sphere at some locations due to the obstruction caused by the support vanes. Figure 3.16 shows an irradiance pattern measured by the detector at the output of the lens and an intensity pattern measured at the output of the integrating sphere to demonstrate these differences.

A final iteration of simulating the optical model with different conical baffle base widths was performed to ascertain the conical baffle size that produced the best overall system output. It was determined that the conical baffle base width that generated the most uniform system output was 7.44 mm. The simulation results for the system output with this configuration of the model are shown in Fig. 3.17.

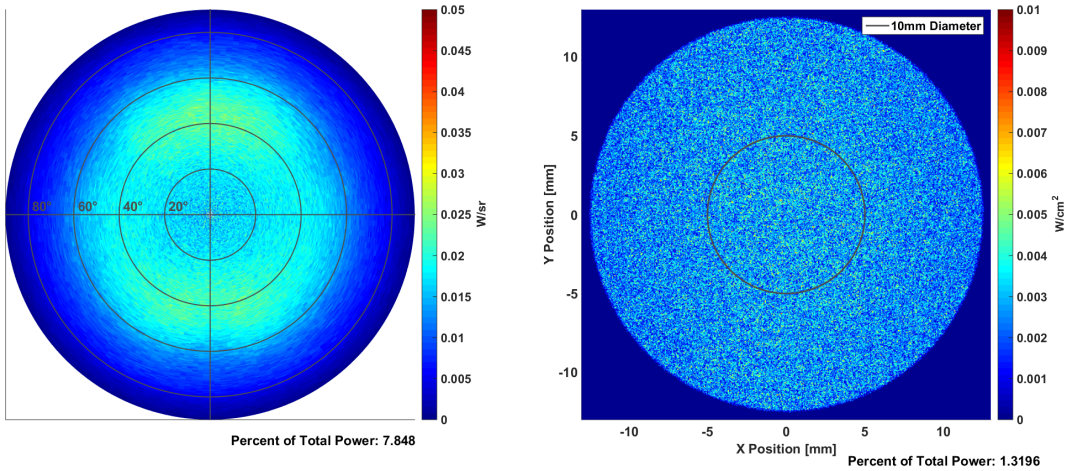

(a) Integrating sphere output intensity. (b) Lens output irradiance.

Fig. 3.16: Detector images with spider support vanes added to the model, and a separation added between the QCL and the conical light pipe.

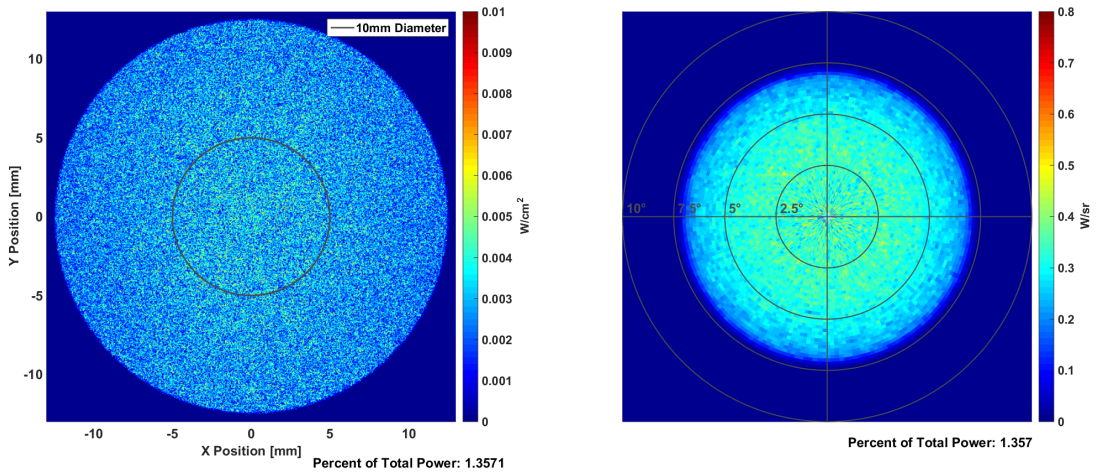

(a) Lens output irradiance. (b) Lens output intensity.

Fig. 3.17: Detector images at the output of the lens with conical baffle base width of 7.44 mm.

3.5 Model Dimensions Based on Actual Hardware

In the process of making mechanical drawings for the conical light pipe, the design was modified to include a 0.4-mm cylindrical lip at the entrance port. This lip was added to aid in machining. A number of simulations were performed to determine the tolerances for

the fabrication of the hardware. Once these tolerances were known, they were added to the mechanical drawings and the hardware was machined in the machine shop at Space Dynamics Laboratory (SDL). The conical baffle and integrating sphere were coated with Infragold by Labsphere as planned. The conical light pipe, with a quasi-specular reflective interior surface, was gold plated by Quality Plating. After the hardware for the conical baffle, integrating sphere, and conical light pipe had been machined and coated the components were measured to find their actual dimensions. All of the dimensions except for the length of the conical baffle were within design tolerances. The length of the conical baffle was slightly shorter than the design. The optical model was modified to match the dimensions of the actual hardware, and the output of the source system was simulated again. The simulation results for the integrating sphere and lens output are shown in Figures 3.18 and 3.19.

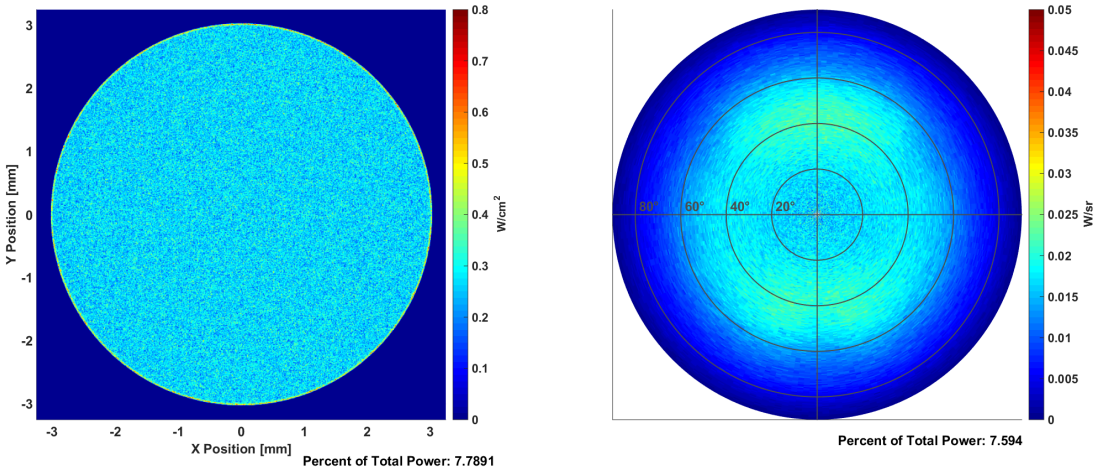

(a) Sphere output irradiance.

(b) Sphere output intensity.

Fig. 3.18: Detector images at the output of the integrating sphere with model dimensions matching actual hardware.

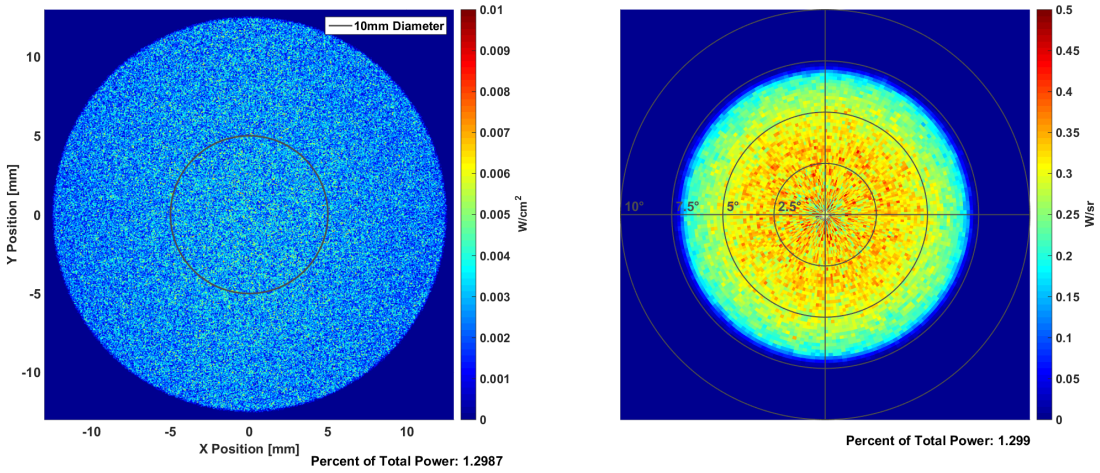

(a) Lens output irradiance.

(b) Lens output intensity.

Fig. 3.19: Detector images at the output of the lens with model dimensions matching actual hardware.

The conical baffle was such a small and fragile part that it could not be coated with Infragold by the standard coating processes. Because of this, the reflectance of the conical baffle was not as diffuse as was desired. A version of the optical model was created that had a specular conical baffle to see how that would affect the output to the system. The simulation results at the sphere output and lens output for this model are shown in Figures 3.20 and 3.21, illustrating that a specular reflection is undesirable.

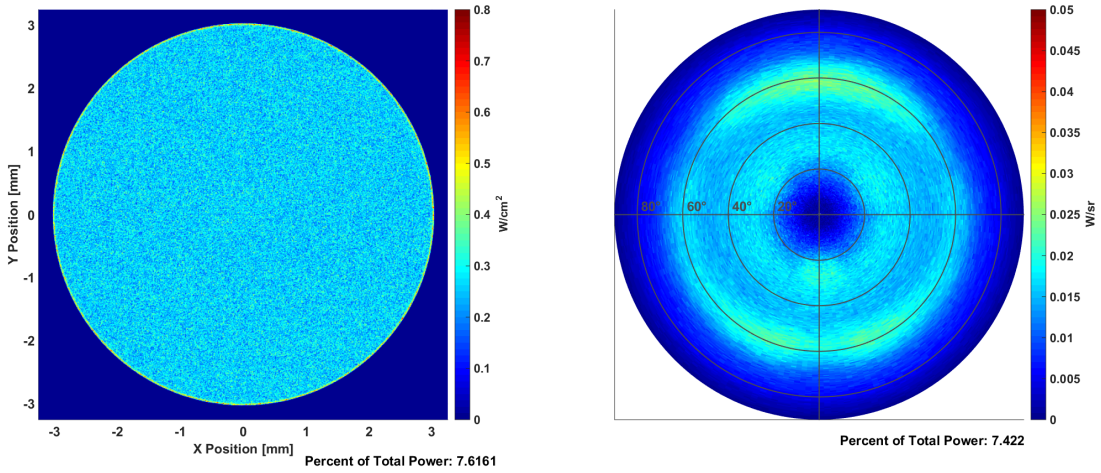

(a) Sphere output irradiance.

(b) Sphere output intensity.

Fig. 3.20: Detector images at the output of the integrating sphere for the model with a specular conical baffle.

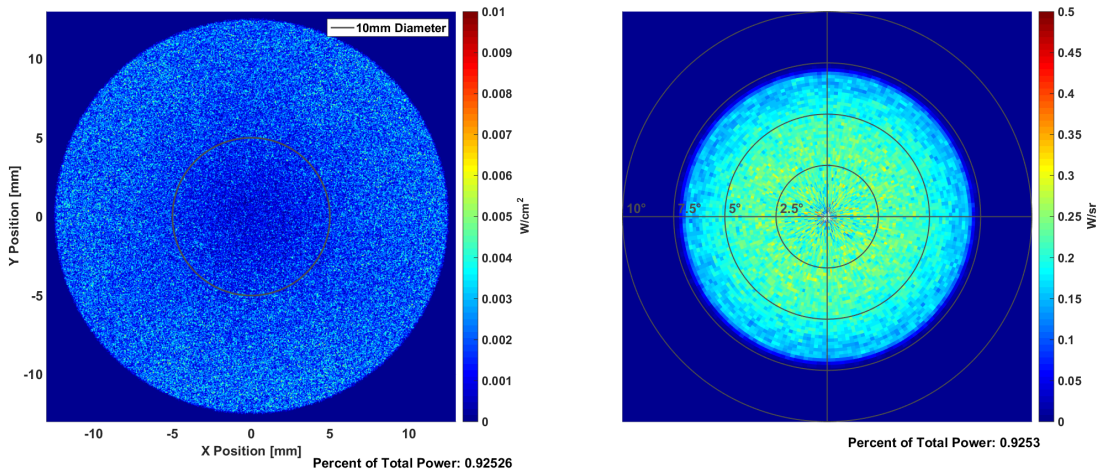

(a) Lens output irradiance.

(b) Lens output intensity.

Fig. 3.21: Detector images at the output of the lens for the model with a specular conical baffle.

3.6 Output Aperture and Lens Options

As previously mentioned, only the central 10 mm of the beam was to be used for calibration. Therefore, the 25-mm beam is larger than necessary. A 15-mm aperture was added on the flat side of the lens to limit the beam diameter. The 15-mm aperture ensures

that the entire 10-mm beam of interest exits the system, while limiting the beam size to remove a portion of it that is not of importance for calibration purposes.

Initially a silicon plano-convex lens was selected for the design because it was relatively inexpensive and readily available. However, using a plano-convex lens results in some spherical aberration in the output beam. A few different achromatic doublets and an aspherical lens were considered as candidates to use for the lens in the system because they would remove the spherical aberration from the output beam. Each lens considered was simulated to see if it would improve the uniformity of the output beam exiting the system. The simulation results showed that there was not a noticeable improvement in beam uniformity when using the achromatic doublets or the aspherical lens. Therefore, the silicon plano-convex lens was selected for the final system design. After the lens was selected, this design was established as the baseline design that would be implemented in hardware. Simulation results for the baseline design are shown in Figures 3.22 and 3.23.

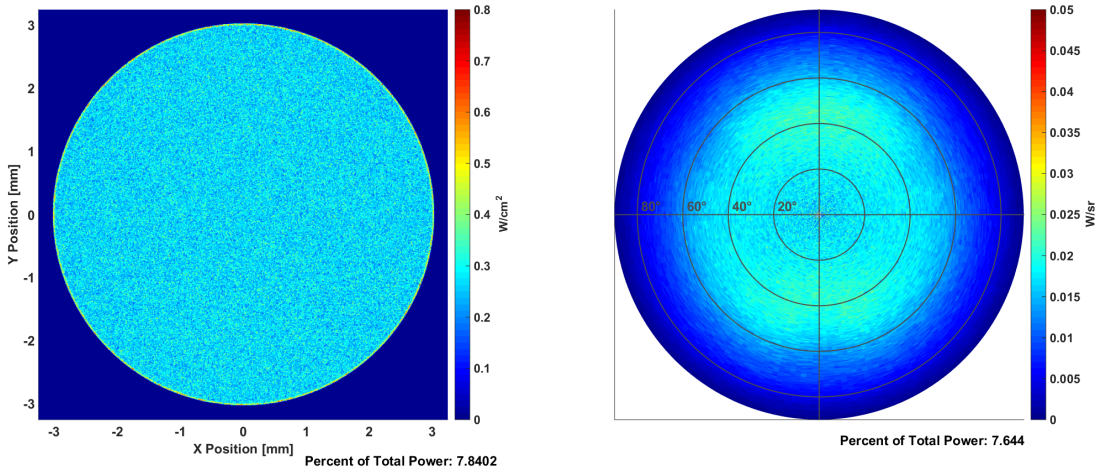

(a) Sphere output irradiance.

(b) Sphere output intensity.

Fig. 3.22: Detector images at the output of the integrating sphere for the baseline design model.

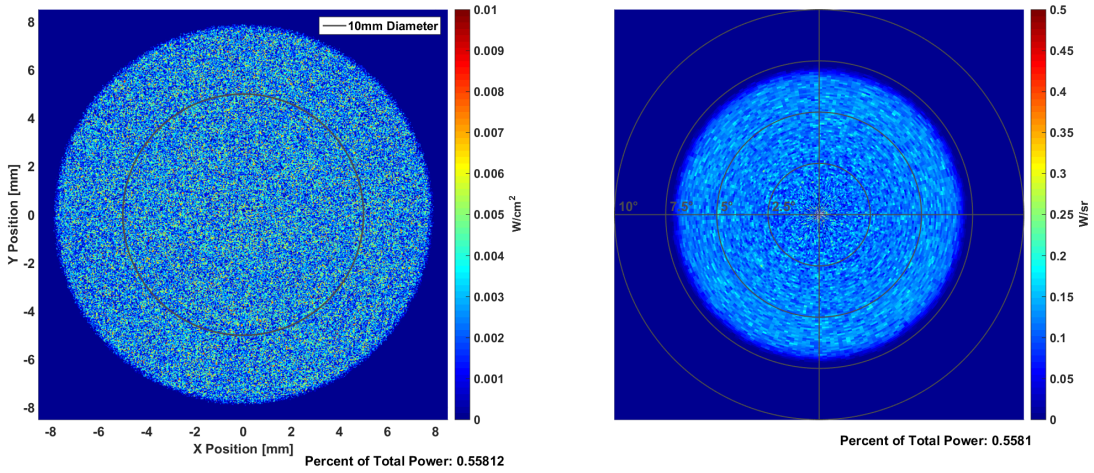

(a) Lens output irradiance.

(b) Lens output intensity.

Fig. 3.23: Detector images at the output of the lens for the baseline design model.

3.7 Output Compound Parabolic Concentrator Instead of Lens

The optical model for the baseline design was inefficient, with 0.56% of the input optical power making it through the system, and only 0.24% of the input optical power contained in the 10-mm diameter beam of interest. Pacific Northwest National Laboratories (PNNL) is a collaborator on this project. They suggested replacing the lens and baffle system at the output of the integrating sphere with an inverted CPC in order to improve the efficiency of the system. Having a CPC on the output would ensure the that all of the energy that is output from the integrating sphere is directed into the calibration beam. The trade-offs for this are that the CPC would have to be very long in order to produce the same FOV on the output, and CPCs are expensive because they are difficult to fabricate.

An inverted CPC at the output of the integrating sphere was simulated to compare with the baseline design. A CPC approximately 20 cm long was required in order to produce an output beam divergence of 15°. This CPC was easy to model but was impractical to implement in hardware. The simulation results for the model with the CPC at the output are shown in Fig. 3.24. The output beam is significantly larger with the CPC on the output of the system. The larger output beam is spatially non-uniform, but the central 10-mm diameter of the beam is relatively uniform and may be acceptable for use in calibration.

Using a CPC on the output makes the overall system more efficient, with 6.16% of the input optical power making it to the output detector, however, the 10-mm diameter beam of interest only contains 0.29% of the input optical power. Using a CPC at the output of the integrating sphere only slightly increases the efficiency of the system, and is more complex to implement than using a lens at the output.

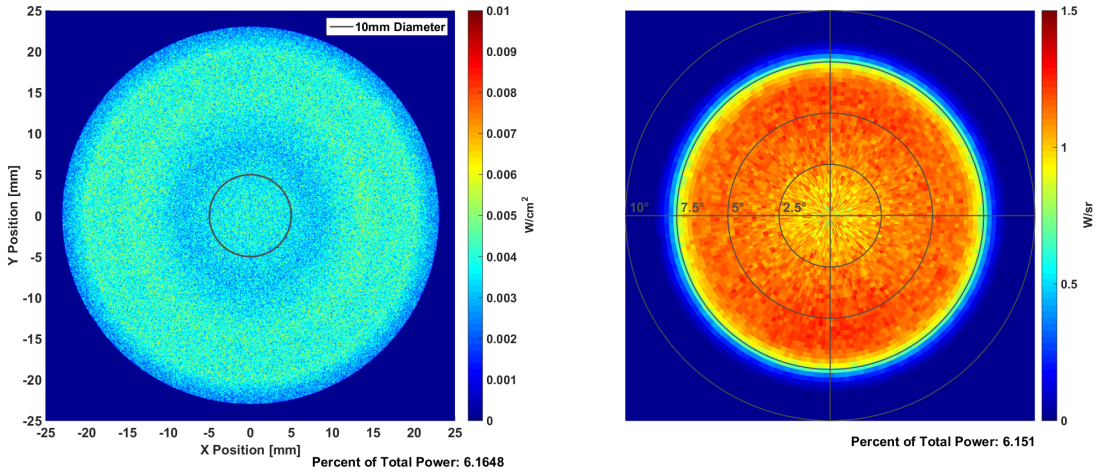

(a) CPC output irradiance.

(b) CPC output intensity.

Fig. 3.24: Detector images at the output of the CPC.

Chapter 4

Hardware Implementation and Testing

4.1 QCL Source System Test Assembly

The hardware components were assembled and aligned in preparation for testing. Figure 4.1 illustrates a computer-aided design (CAD) model of the QCL source system assembly that was used for the tests. This source system assembly consists of the M1013AU QCL, the LDM-4872 QCL mount, the beam conditioning optics, and the mechanical structure that holds the components in proper alignment.

The QCL was driven by the precision current source designed by Hansen [8]. This precision current source was designed to output one of sixteen discrete current levels based on user defined set points.

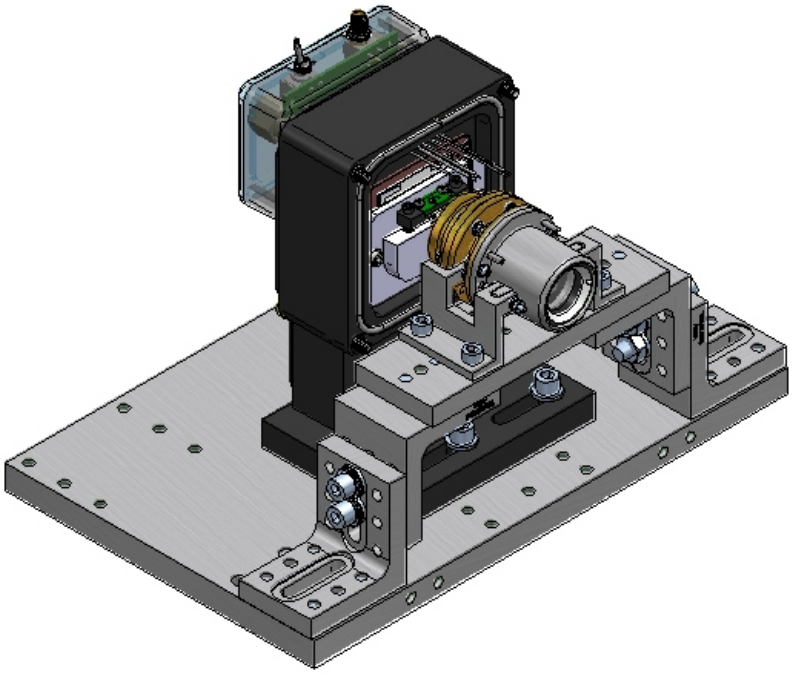

Fig. 4.1: QCL source system assembly.

4.2 Purpose of Hardware Tests

Two main sets of tests were collected in order to characterize the system in terms of the following characteristics:

1. The stability of the source system over time.
2. The uniformity of the output beam from the system.
3. The relative spectrum of the output beam from the system.
4. The absolute radiance from the source system.

The first set of tests were performed in an ambient temperature and pressure environment. The second set of tests were performed in a thermal vacuum chamber. The purpose of these tests was to measure each of the characteristics of interest at a set of different operating conditions, in order to characterize the output beam from the source system.

The QCL was operated at four different modes throughout the tests by modulating the current through it at different frequencies. The modes of operation were 20 kHz, 40 kHz, 60 kHz, and continuous wave (CW). The QCL was operated at one or more of these modes during each test. The following two sections detail the modes of operation for each test.

4.3 Ambient Testing Overview

The system was tested with the QCL operating at each of the four modulation modes at ambient temperature and pressure as outlined in Table 4.1. Detailed descriptions of each of the test configurations are given in the next four subsections.

Table 4.1: QCL modulation modes for each ambient test configuration.

QCL Temperature [°C]	**QCL Mode [kHz]**				
	Stability Test	**Uniformity Test**	**Polarization Test**	**Relative Spectral Output Test**	**Radiance Calibration Test**
10				CW, 20, 40, 60	
20	CW, 20, 40, 60	CW, 20, 40, 60	CW, 20, 40, 60	CW, 20, 40, 60	CW, 20, 40, 60
30				CW, 20, 40, 60	
40				CW, 20, 40, 60	

4.3.1 Stability Test

The QCL source system was mounted on an optical breadboard and aligned with a power meter as shown in Fig. 4.2a. Figure 4.2b shows the system after it was encapsulated in a foam container which was designed to minimize temperature fluctuations in the system throughout the stability test. One iteration of the ambient stability test consisted of stepping the QCL through each of the sixteen power levels for thirty seconds each. At the end of each iteration the current through the QCL was set to zero for one-hundred and fifty seconds to allow its temperature to stabilize before the next iteration. One-hundred and forty-four iterations of data were collected for each of the modes outlined in Table 4.1.

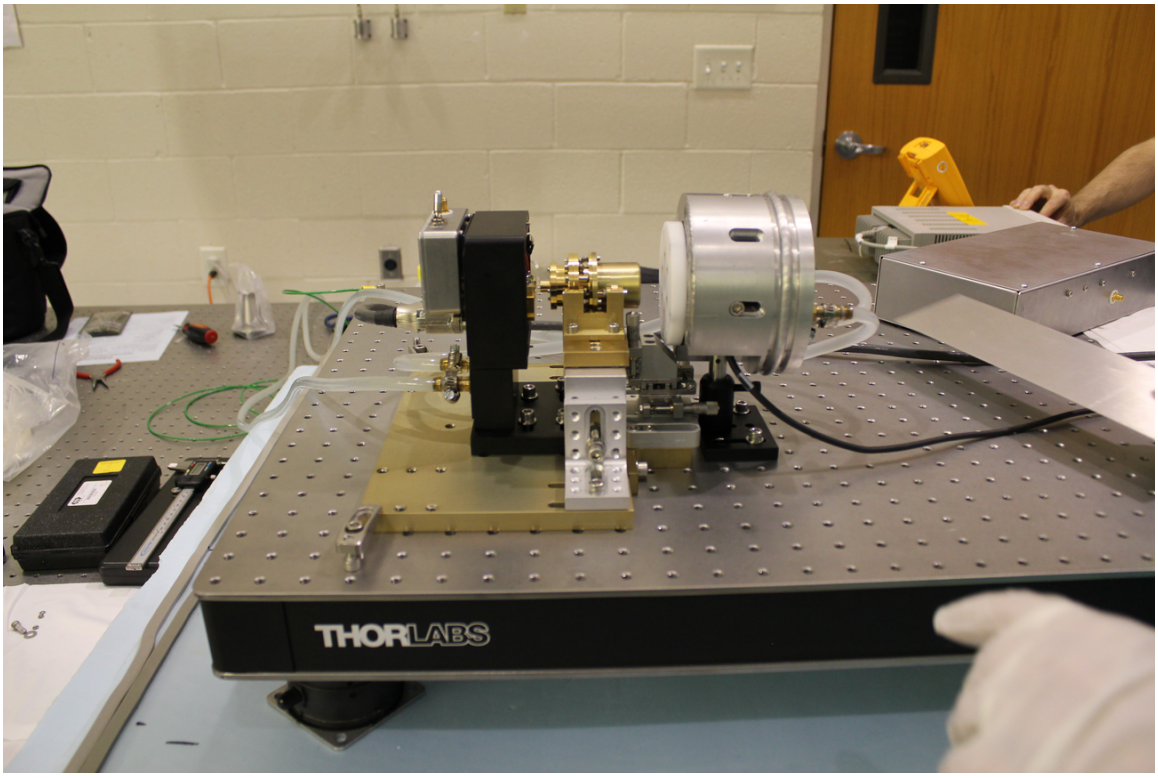

(a) QCL source system assembly.

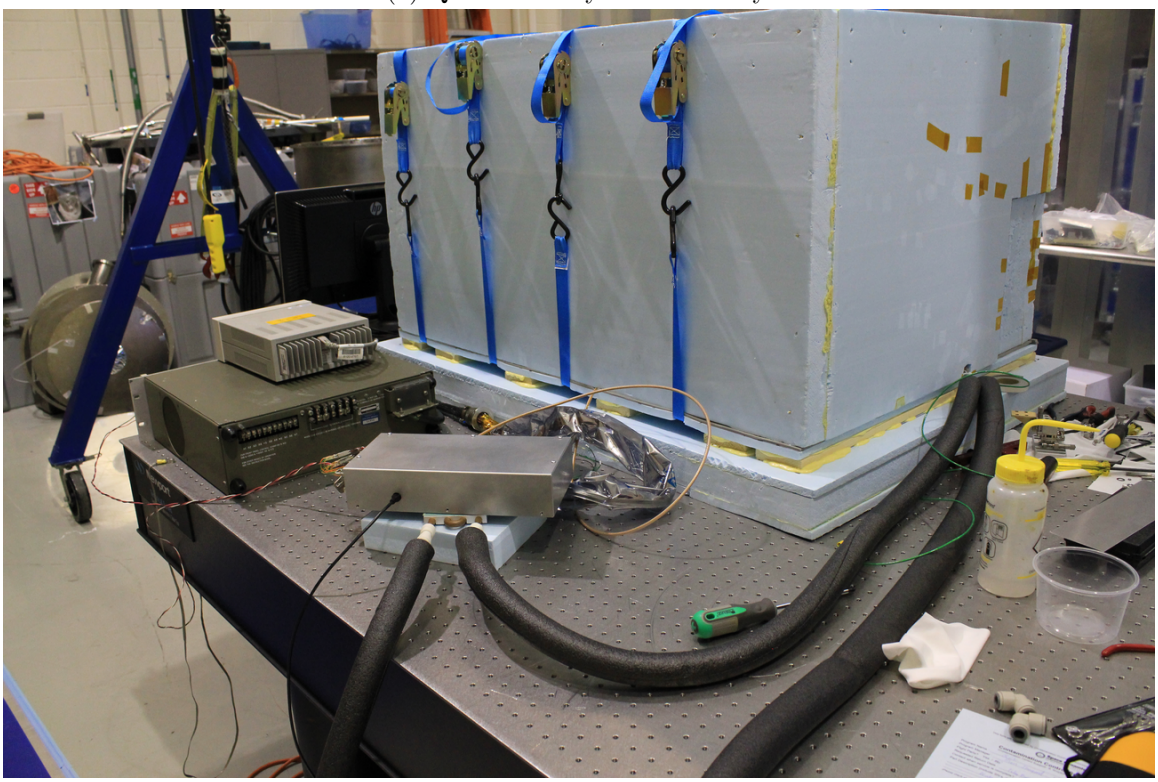

(b) QCL source system assembly enclosed in foam container.

Fig. 4.2: Ambient stability test hardware configuration.

4.3.2 Relative Spectral Output Test

An interferometer was aligned with the source system as shown in Fig. 4.3. Spectral data was collected for each of the modes outlined in Table 4.1. A measurement of a blackbody with a known temperature was made prior to and after the spectral measurements of the source system. This allowed blackbody measurements to be used to calculate the interferometer's response so it could be removed from the spectral data.

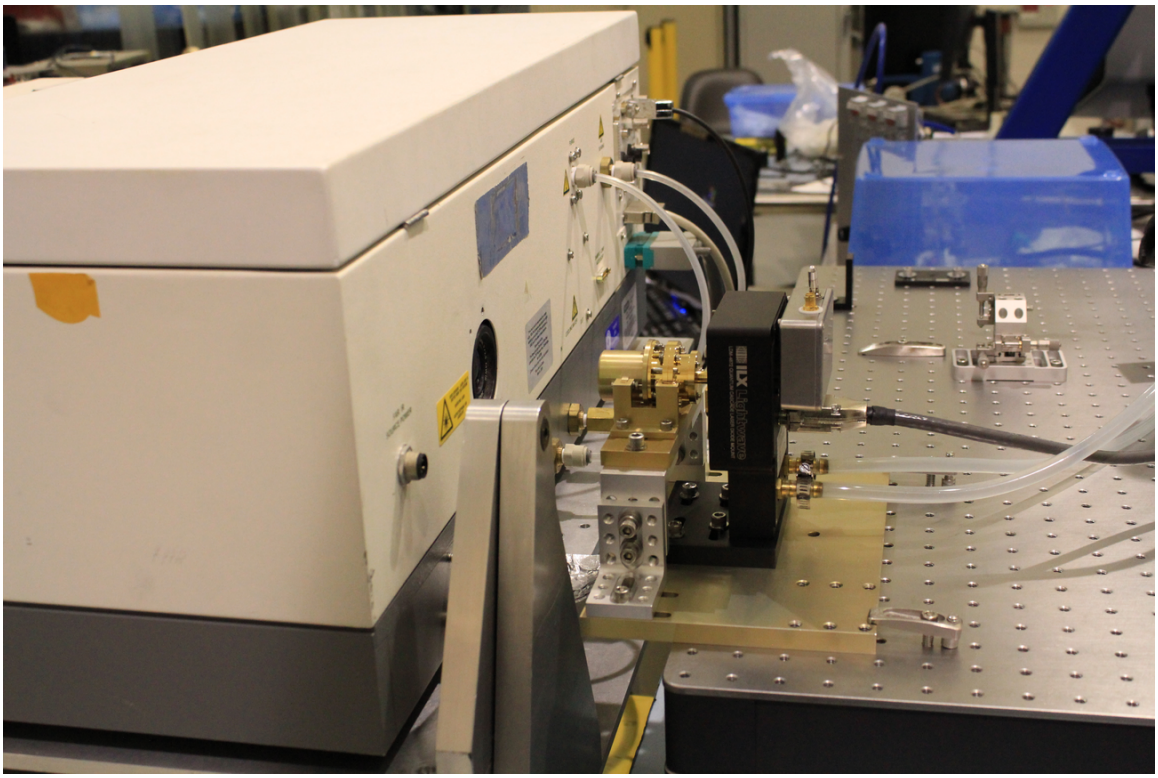

Fig. 4.3: Hardware configurations for the ambient relative spectral output test.

4.3.3 Output Beam Uniformity Test

For the output beam uniformity test an infrared (IR) camera was aligned with the source system as shown in Fig. 4.4. The IR camera used for the ambient tests used a bandpass filter centered on the wavelength of the QCL. This was done in order to minimize the amount of background noise in the measurements. Data was collected with three different lenses at two different focus configurations. The lenses used had focal lengths of 25 mm, 50 mm, and 100 mm. Data was collected with each of the lenses focused on the output from

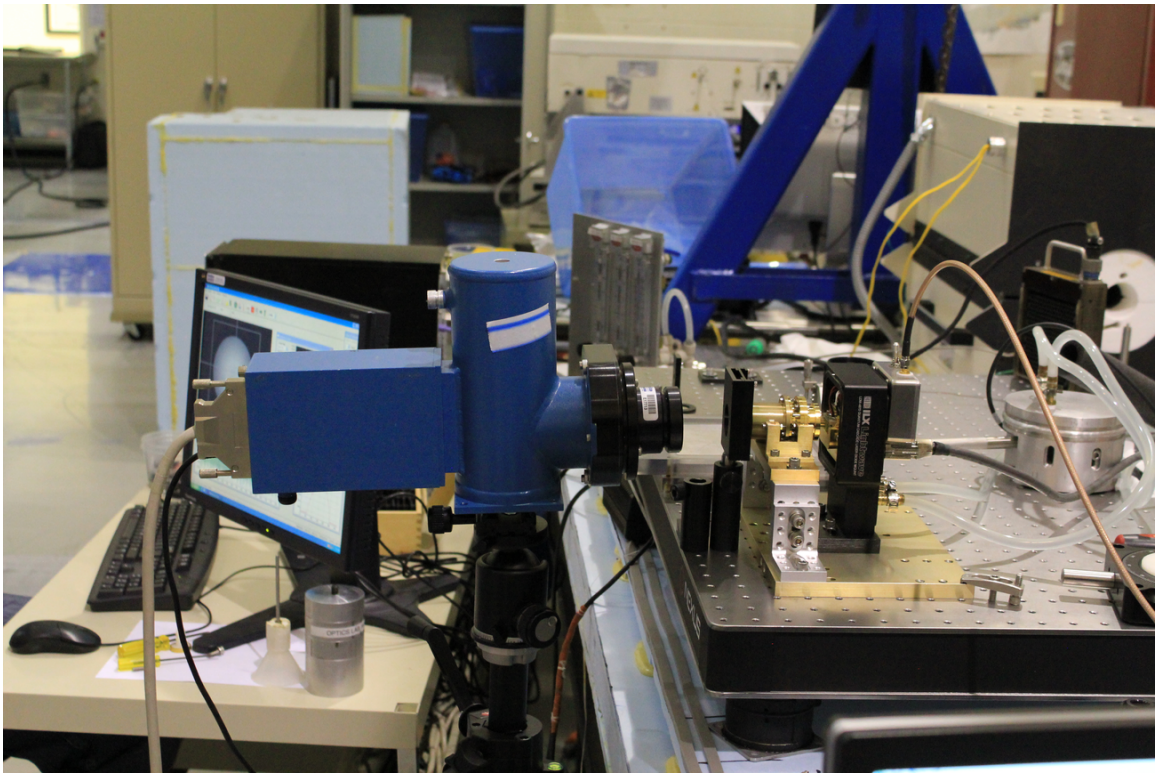

Fig. 4.4: Hardware configuration for the ambient output beam uniformity test.

the integrating sphere aperture to measure the angular uniformity of the beam, and with each of the lenses focused on the output from the lens to measure the spatial uniformity of the beam.

4.3.4 Radiance Calibration Test

For the radiance calibration test a power meter was used to measure the power output from both a calibrated blackbody and the QCL source system. Both of those measurements were needed in order to calculate the absolute radiance from the QCL source system. A detailed description of that calculation is given in Chapter 5. Figure 4.5 shows the hardware configuration for the measurement of the blackbody during the ambient radiance calibration test. The hardware configuration for measuring the power output from the QCL source system was the same as shown in Fig. 4.2a for the stability test.

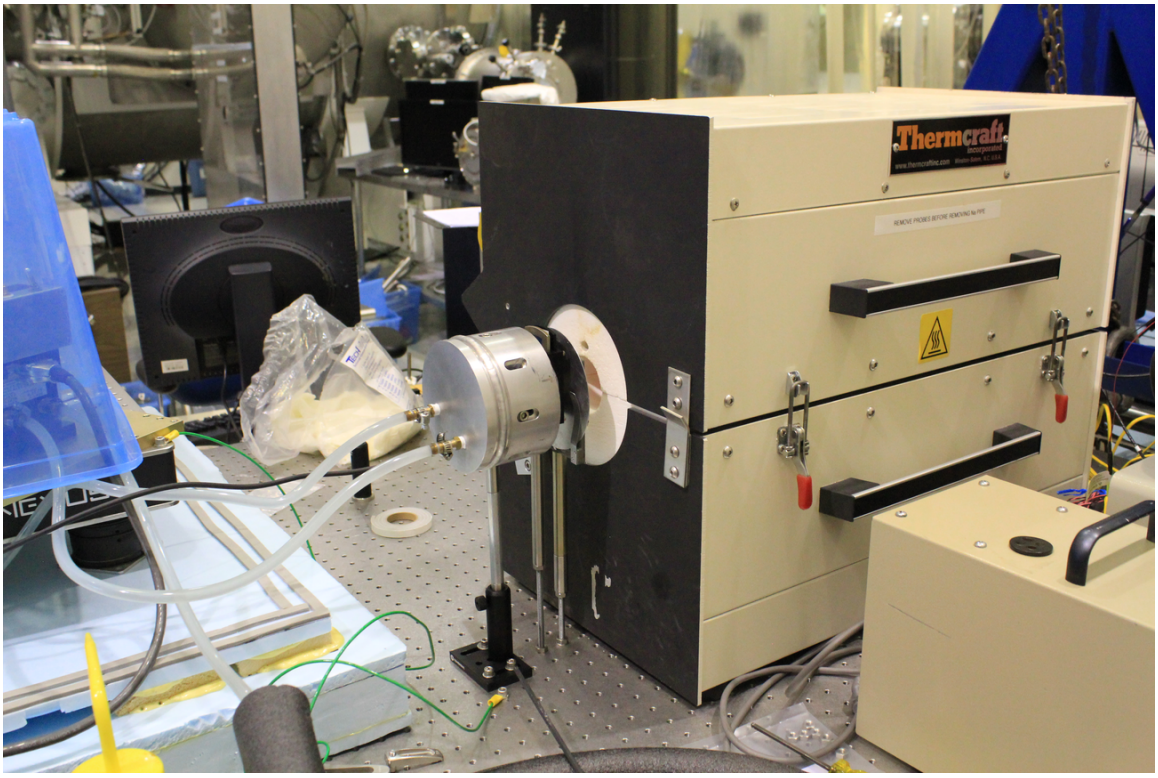

Fig. 4.5: Hardware configuration of the blackbody measurement setup for the ambient radiance calibration test.

4.4 Thermal Vacuum Testing Overview

The QCL source system assembly was mounted inside a dewar for the thermal vacuum tests. Figure 4.6 shows a drawing of the QCL source system assembly mounted inside of the dewar. Table 4.2 outlines the modulation modes the QCL was operated at for each of the tests that were performed while the system was in the thermal vacuum chamber. A description of the hardware configuration for each of the thermal vacuum tests is outlined in the next four subsections.

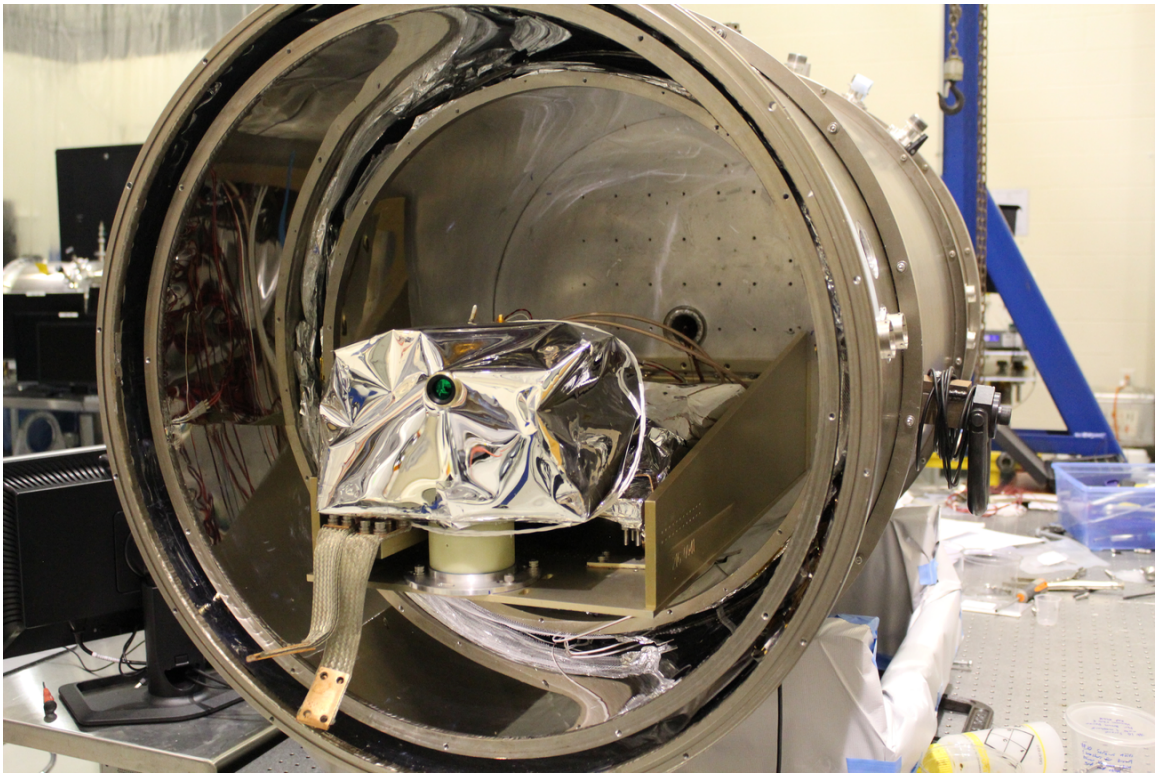

Fig. 4.6: QCL source system thermal vacuum assembly.

Table 4.2: QCL modulation modes for each thermal vacuum test configuration.

QCL Temperature [°C]	**QCL Mode [kHz]**				
	Stability Test	**Uniformity Test**	**Polarization Test**	**Relative Spectral Output Test**	**Radiance Calibration Test**
20	CW, 20, 40, 60	CW, 40	CW, 40	CW, 20, 40, 60	CW, 40
-10	CW, 40, 60	CW, 40		CW, 20, 40, 60	
-40	CW, 40, 60	CW, 40		CW, 20, 40, 60	
-40	CW, 40				
-40	CW, 40, 60	CW, 40		CW, 20, 40, 60	
-Min Temp	CW, 40			CW, 20, 40, 60	

4.4.1 Stability Test

As shown in Table 4.2, the stability test was performed at each selected temperature while the system was in the thermal vacuum chamber. The power meter used for the stability test measurements was mounted outside the dewar. A foam box was constructed and mounted around the power meter as shown in Fig. 4.7 to help keep the temperature of the power meter constant. A tent made of orcofilm was hung over the power meter and the dewar as shown Fig. 4.8 to reduce reflections from the surrounding environment and the flow of air currents between the output beam from the source system and the power meter.

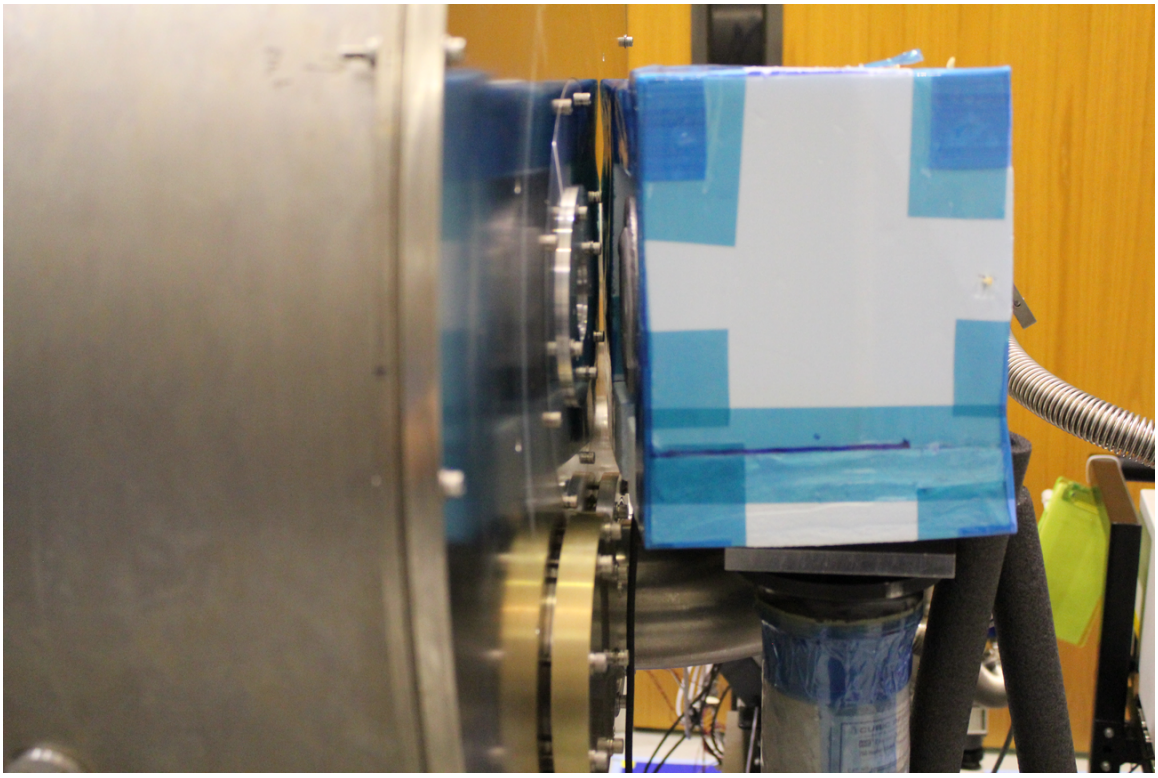

Fig. 4.7: Power meter enclosed in a foam box to help with temperature stability.

This tent greatly reduced the background noise seen by the power meter. Figure 4.9 is a plot of the power meter readings before and after the tent was put in place. The reduction in noise is clearly visible in the plot.

One iteration of the vacuum stability test consisted of operating the QCL on each of sixteen power levels for ninety seconds each. The reason for the vacuum test having a longer step time than the ambient test is because the QCL heat sink in the vacuum was not as efficient at dissipating the heat from the QCL as the heat sink in the ambient test. As in the ambient stability test, at the end of each iteration the current through the QCL was set to zero for a period of time to allow its temperature to stabilize before the next iteration. Twelve iterations of data were collected for each of the modes outlined in Table 4.2.

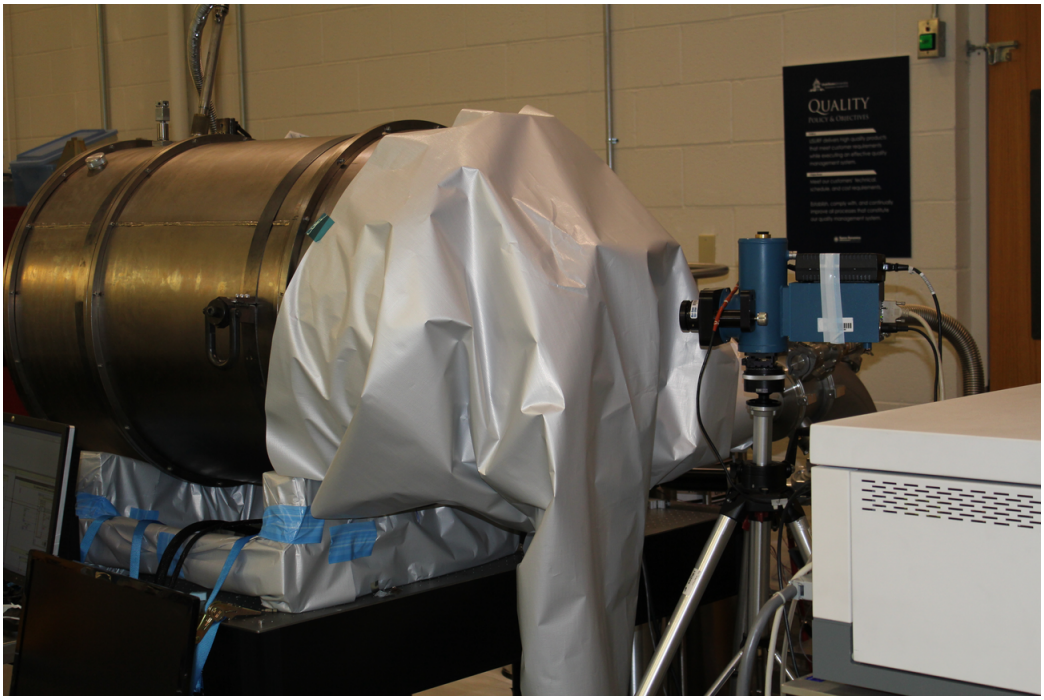

Fig. 4.8: Orcofilm tent hung over the power meter to reduce air flow between the power meter and the dewar.

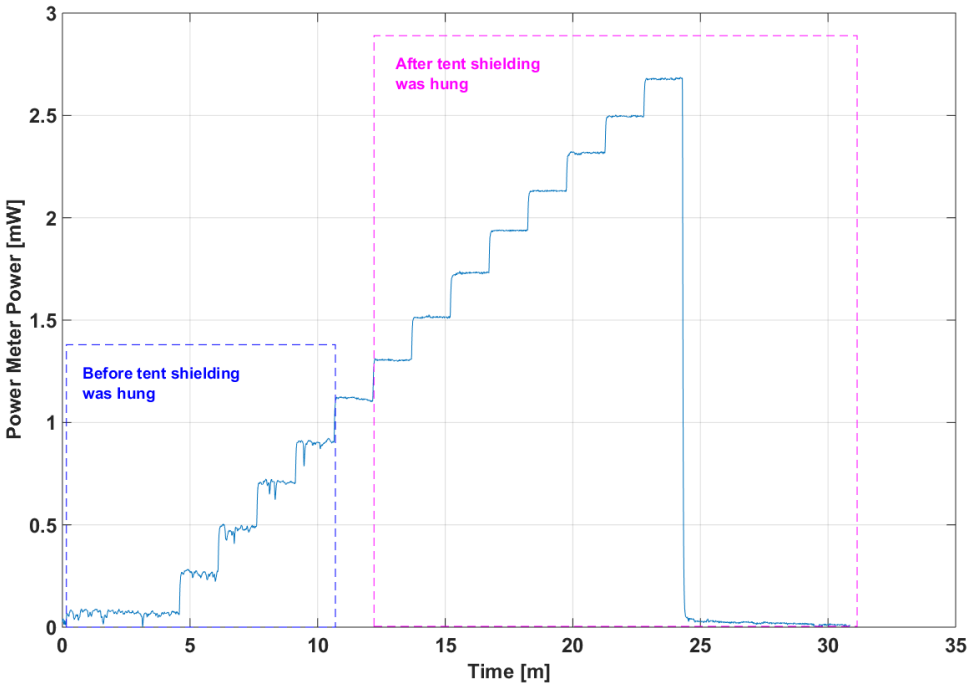

Fig. 4.9: Plot showing the effect of the orcofilm tent on the power meter readings.

4.4.2 Relative Spectral Output Test

An interferometer was aligned with the source system through the dewar window for the relative spectral output tests in thermal vacuum. Spectral measurements were collected with the QCL operating at power levels 4, 10, and 15 for all four modulation modes. Similar to the ambient relative spectral output test, a measurement of a blackbody with a known temperature was made at each temperature configuration. This was done so that the data from blackbody could be used to calculate the interferometer's response. Once the interferometer's response was known it was subtracted from the collected data.

4.4.3 Output Beam Uniformity Test

An IR camera was aligned with the source system to collect data for the output beam uniformity test. Data was collected with both a 50-mm focal length lens and a 25-mm focal length lens while the camera was focused on two different locations. The first focus location was the output aperture from the integrating sphere. This focus was used to collect the angular beam uniformity data. The second focus location was the lens. This focus was used to collect the spatial uniformity data. For these tests, the QCL was operated at power levels 10 and 15 for the modes outlined in Table 4.2.

4.4.4 Radiance Calibration Test

As in the ambient tests, the radiance calibration test required two different data measurements in order to have the needed data to calculate the absolute radiance from the QCL source system. The first set of data measured the power output from a calibrated blackbody with a known radiance, and the second set of data measured the power output from the QCL source system. Both measurements were made with the power meter. Figure 4.10 shows the hardware configuration for the measurement of the blackbody. The hardware configuration for the source system power measurements was the same as the configuration for the stability test shown in Figures 4.7 and 4.8.

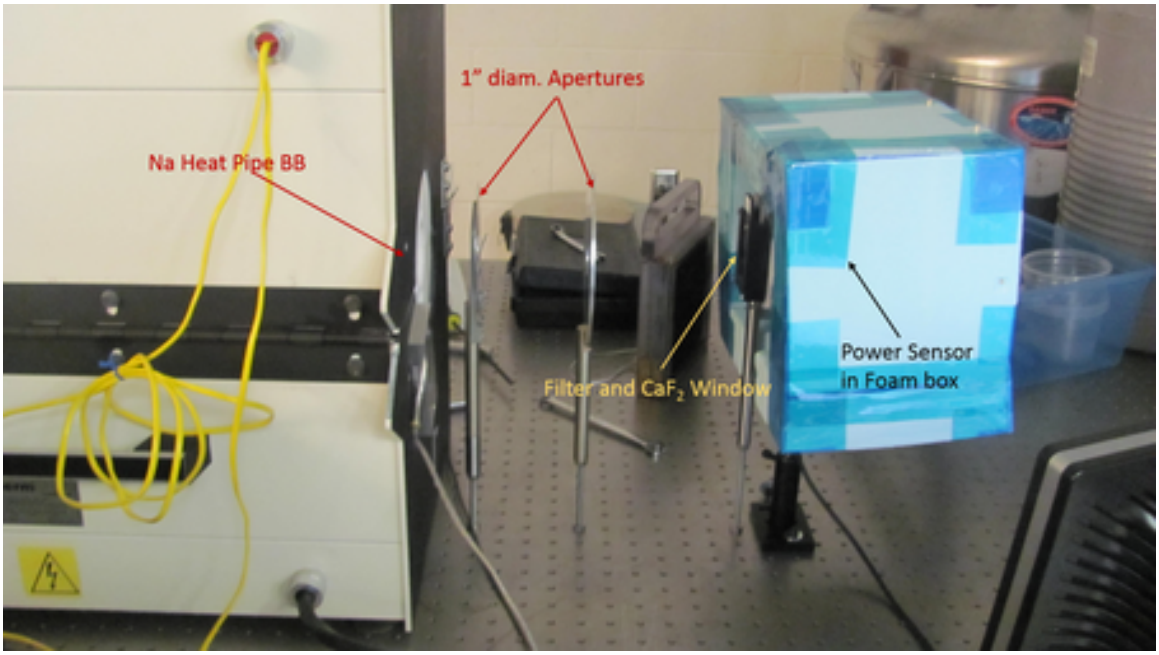

Fig. 4.10: Hardware configuration for blackbody measurements for the thermal vacuum radiance calibration test.

Chapter 5

Hardware Test Data Processing and Analysis

5.1 QCL Modulation Modes

An outline of the data that was collected is given in Tables 4.1 and 4.2. Testing was performed with the QCL operating at the four different modulation modes of 20 kHz, 40 kHz, 60 kHz, and CW in order to ascertain if one particular mode of operation was better than another in terms of QCL output power stability. Tests performed by PNNL demonstrated that the QCL power output is more stable when the QCL is modulated than when it is operating in CW mode [15]. The CW mode data was collected in order to obtain a complete characterization of the QCL source system; however, the operating modes of interest are those in which the QCL is modulated. After processing the data it was realized that there is no noticeable difference seen from modulating the QCL at higher or lower frequencies. Because of this, the data presented in this chapter is going to mainly focus on data collected with the QCL operating in the 40 kHz modulation mode.

5.2 Data Analysis

The data analysis processes for both the ambient tests and the vacuum tests are nearly identical. Because of this, these processes will only be described once, and the data plots from both sets of tests will be presented simultaneously.

The precision current controller used to drive the QCL was characterized at SDL in a set of tests in which its output current was measured. The configuration of the hardware in the tests described in this thesis did not allow a sensor to be put in place to measure the output current from the precision current controller. Due to the lack of actual current measurements for these tests, all of the figures in this chapter that report current data

are showing the average current measured from the precision current source during its characterization.

5.2.1 Stability Test

Figure 5.1 shows the plots of the power meter stability data collected during both the ambient and vacuum tests. The first process performed on the stability data was to remove the background noise measured by the power meter. This was achieved by fitting a polynomial curve to the portion of the data collected when there was zero current through the QCL, and subtracting the polynomial fit from the measured data. The second process performed on the data was a calculation of the average power in each power level step. Only the last ten seconds of each power level step was averaged to ensure that the data in the average was not from the period of time when the QCL temperature was changing, since the QCL power and spectral output are a strong function of temperature. The third process performed on the data was to calculate the average and standard deviation of the average power levels over all of the iterations. The stability of the system is expressed in terms of the percent deviation of each power level over all of the iterations. The percent deviation is calculated by dividing the standard deviation by the average. Figure 5.2 consists of the percent deviation plots for both the vacuum and ambient stability tests.

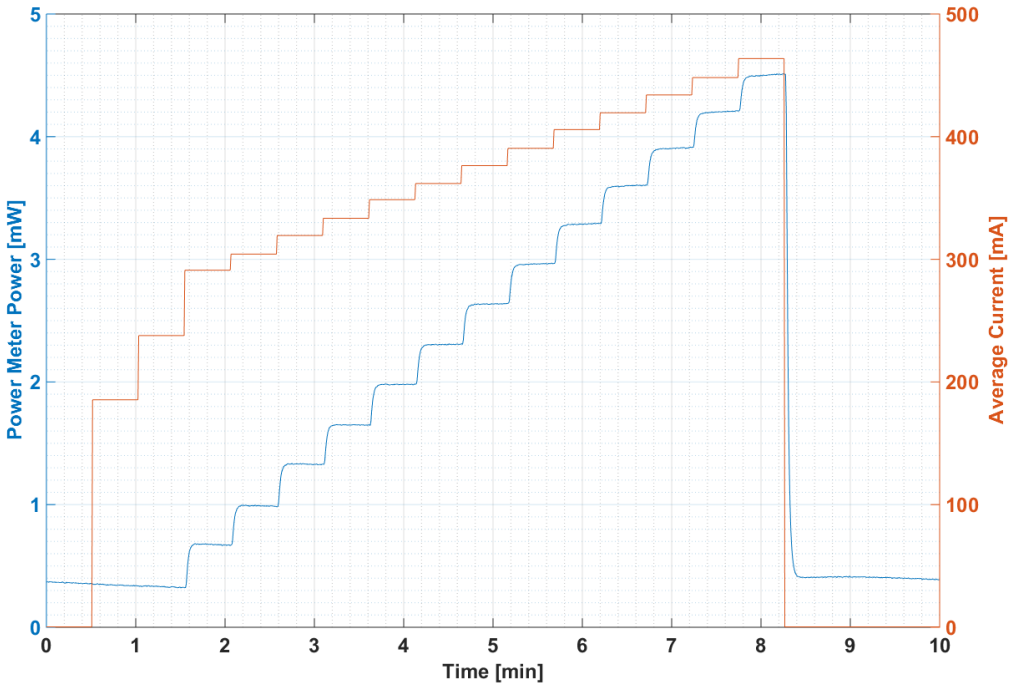

(a) One iteration of ambient stability test data.

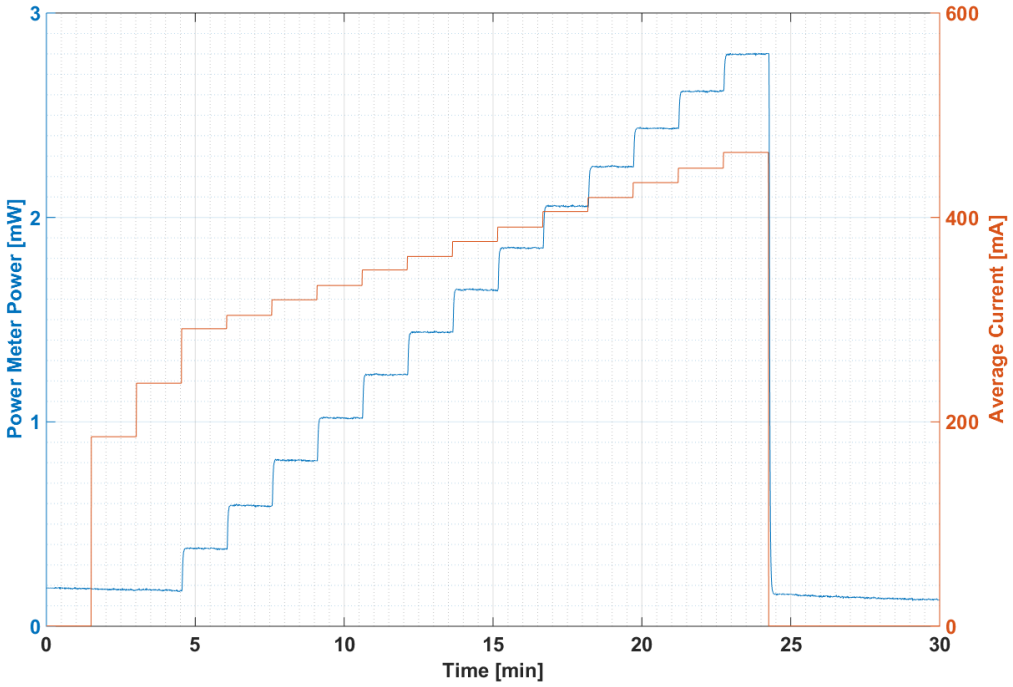

(b) One iteration of vacuum stability test data.

Fig. 5.1: One iteration of raw stability data from each set of tests.

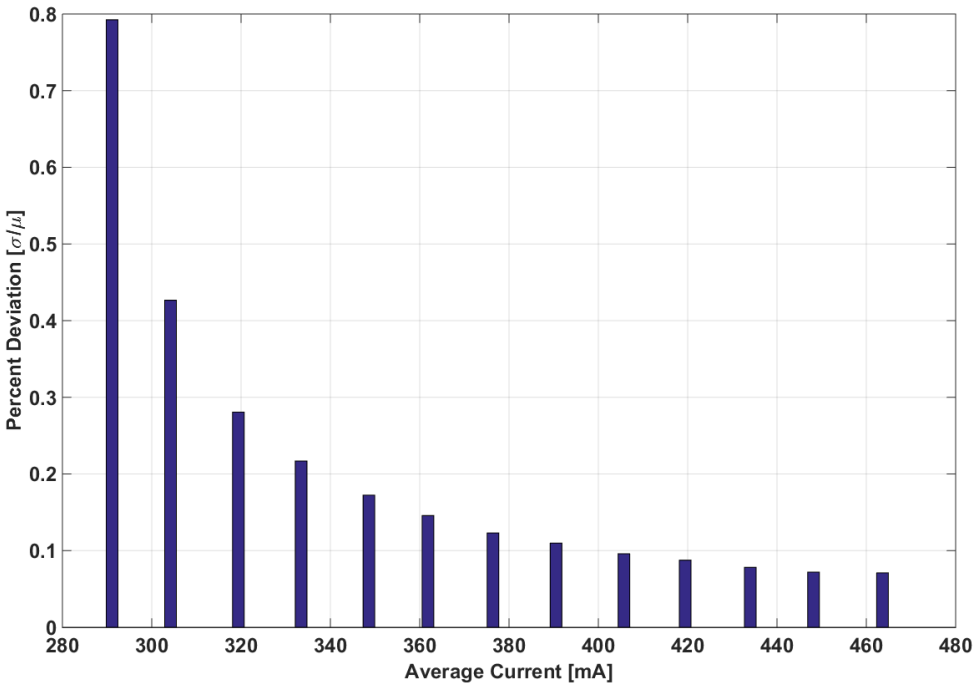

(a) Ambient stability test percent deviation plot.

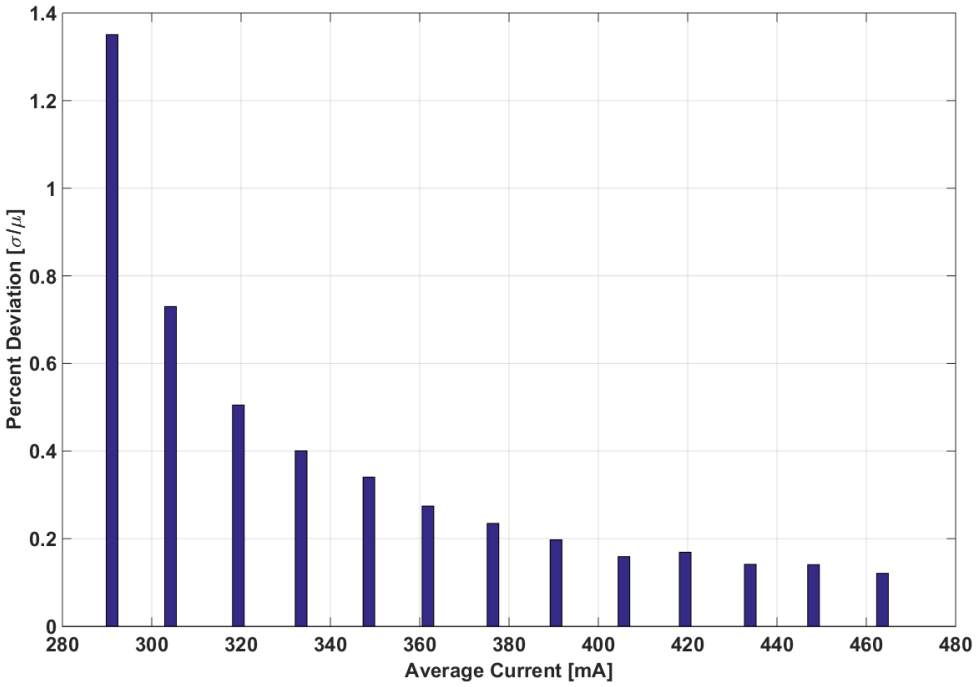

(b) Vacuum stability test percent deviation plot.

Fig. 5.2: Percent deviation each power level over all iterations of the ambient and vacuum stability tests.

5.2.2 Relative Spectral Output Test

The data collected from SDL's FTS 6000 Interferometer was processed by removing the response of the interferometer from the data, and normalizing the data. To remove the response of the interferometer from the data, a calibration constant was calculated using the spectral data collected from a blackbody around the time that the spectral output from the source system was measured. The calibration constant was calculated using the temperature of the blackbody that was measured, and Equation (5.1), which is Planck's Law for electromagnetic radiation emitted from a blackbody in thermal equilibrium, where $B_\lambda(\lambda, T)$ is the spectral radiance of a blackbody, h is the Planck constant, c is the speed of light, λ is the wavelength, k_B is the Boltzmann constant, and T is the temperature of the blackbody [16].

$$B_\lambda(\lambda, T) = \frac{2hc^2}{\lambda^5} \frac{1}{e^{\frac{hc}{\lambda k_B T}} - 1} \tag{5.1}$$

The main purpose of the relative spectral output test was to determine how the output spectrum from the source system varies with respect to temperature and QCL modulation frequency. Figure 5.3 shows the plots of the output of the system from both the ambient and the vacuum tests at different modulation frequencies. The output spectrum from the source system has little variation with different modulation frequencies, however there is a noticeable variation in the output spectrum between operation in CW mode and operation in one of the modulated modes. Since the CW mode is not of primary interest due to its lack of power output stability, it is not a concern that it has a different output spectrum than the modulated modes. Figure 5.4 shows how the spectral output changes with temperature for both the vacuum and ambient tests. It is clear that the spectral output from the system is dependent on QCL temperature. As the temperature decreases, the output spectrum from the system shifts down to shorter wavelengths.

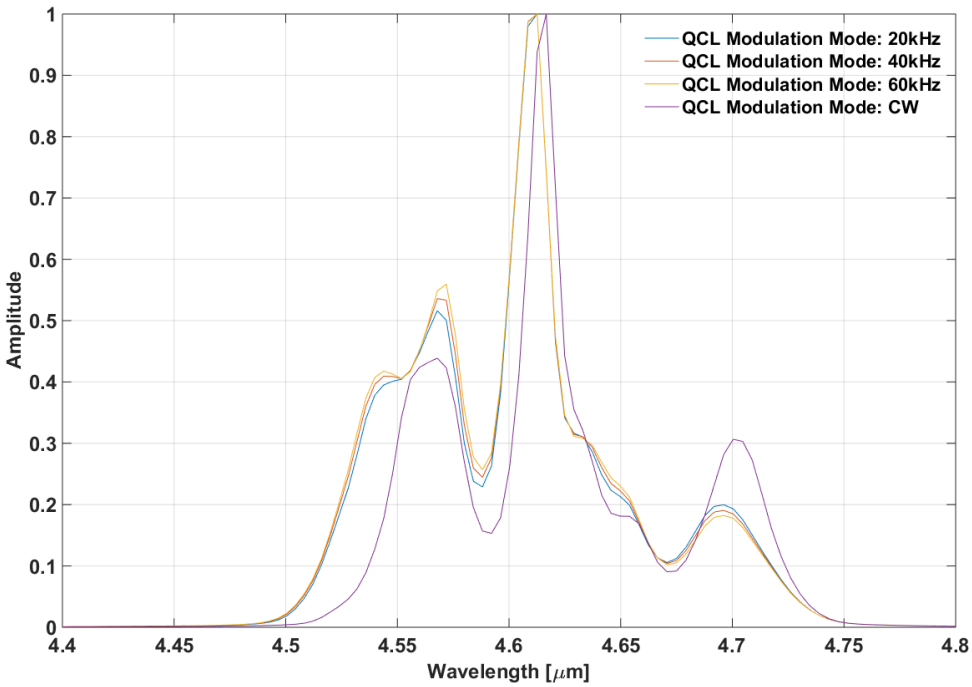

(a) Ambient relative spectral output test plot comparing modulation frequencies.

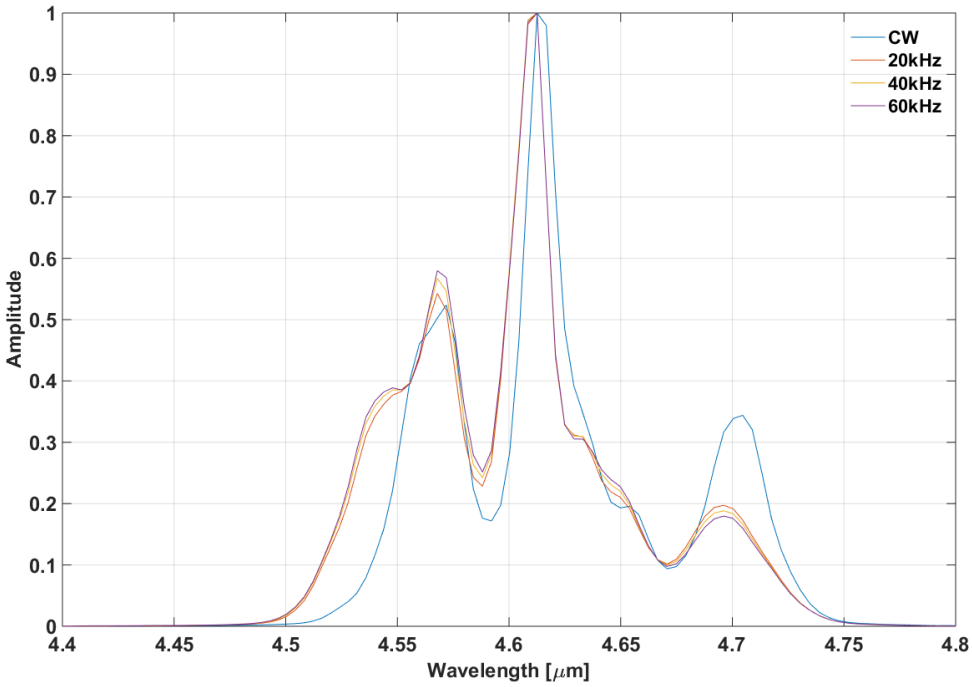

(b) Vacuum relative spectral output test plot comparing modulation frequencies.

Fig. 5.3: Comparison of the change in the relative spectral output with respect to changes in QCL modulation frequencies.

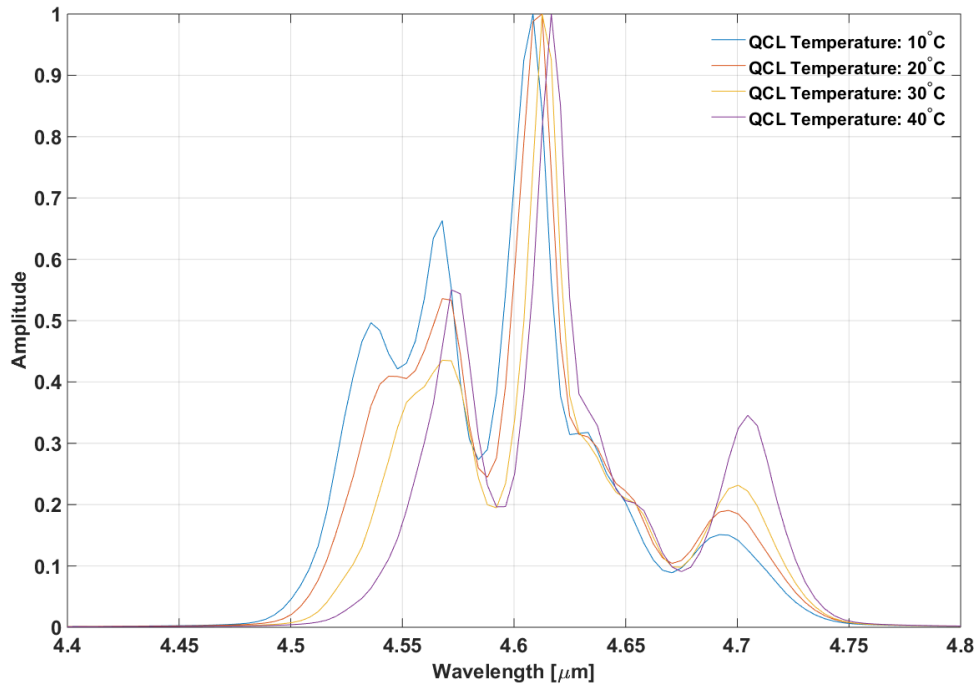

(a) Ambient relative spectral output plot comparing different QCL temperatures.

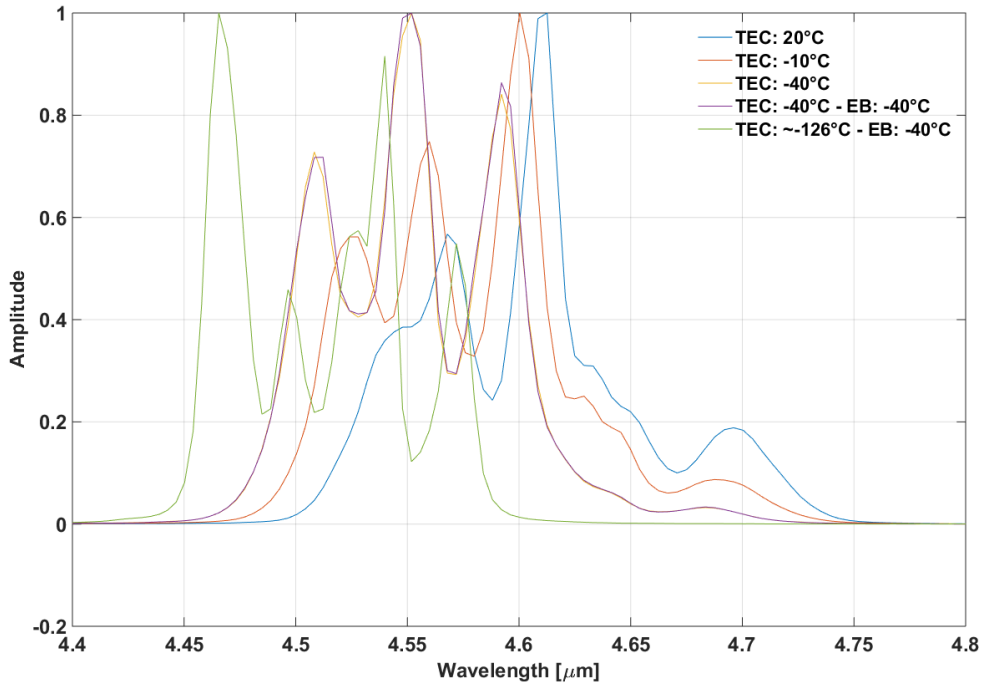

(b) Vacuum relative spectral output plot comparing different QCL temperatures.

Fig. 5.4: Comparison of the change in relative spectral output with respect to changes in QCL temperature.

5.2.3 Output Beam Uniformity

The output beam uniformity data went through three data reduction processes before analysis. The first of these was to apply corrections for offset, gain, and bad pixels in order to correct for the bad pixels in the camera array, and any optical artifacts. The second process was to average each set of 100 frames to reduce the data into a single frame per measurement. The last process was to resize each frame by extracting the pixels centered on the image of the output beam from the QCL source system. Irrelevant pixel data around the outer edge was discarded. A different IR camera was used for the thermal vacuum tests than that used for the ambient tests. Because of this the collected data was in two different formats. However, the data processing steps were essentially the same for both sets of data.

Figure 5.5 shows examples of corrected images from the ambient test, and Figures 5.6 and 5.7 show plots that outline the image correction process for the vacuum tests. Figure 5.5a shows an example of a frame made up of an average of 100 corrected frames, Fig. 5.5b shows the mask used to locate the center of the beam on the image, Fig. 5.5c shows the frame after the unneeded pixels were removed, and Fig. 5.5d shows a cross sectional row of the frame. Figure 5.6a is an image taken of an ambient temperature blackbody source, Fig. 5.6b is an image taken of a 100°C blackbody source, Fig. 5.6c is a gain correction image, Fig. 5.6d is an offset correction image, Fig. 5.6e is an image of the ambient blackbody source after the offset and gain correction has been applied, and Fig. 5.6f is a bad pixel map. Figure 5.7 shows examples of corrected images from the thermal vacuum test. Figure 5.7a shows the raw image of the output beam before correction, Fig. 5.7b shows an image of the output beam after corrections have been applied, Fig. 5.7c shows the frame after the edge pixels not containing data from the output beam were removed, Fig. 5.7d shows a cross section of the corrected frame. The black circle in 5.7c and the red line in 5.7d indicate the 10-mm diameter region of interest of the output beam from the QCL source system.

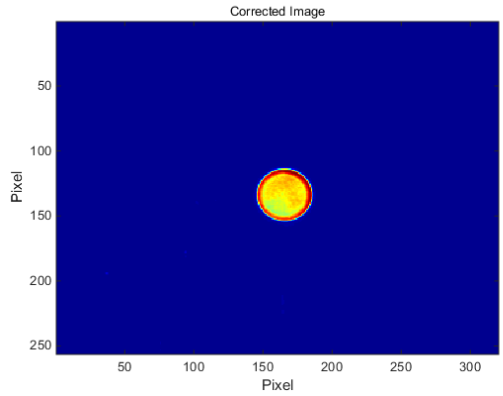

(a) Image of 100 collected frames.

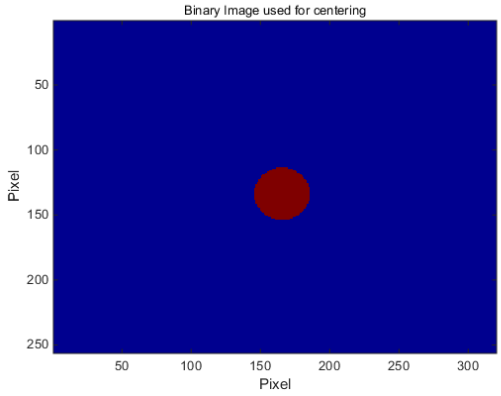

(b) Binary image used to determine beam center.

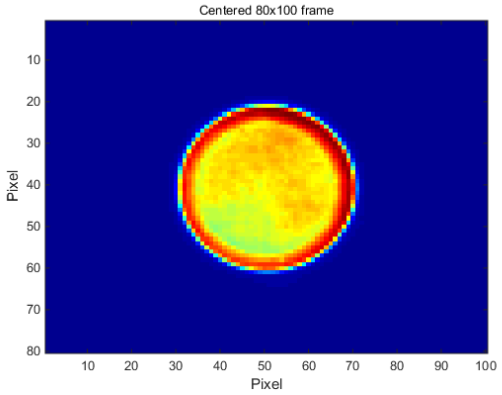

(c) Frame centered on beam with outer edge pixels removed.

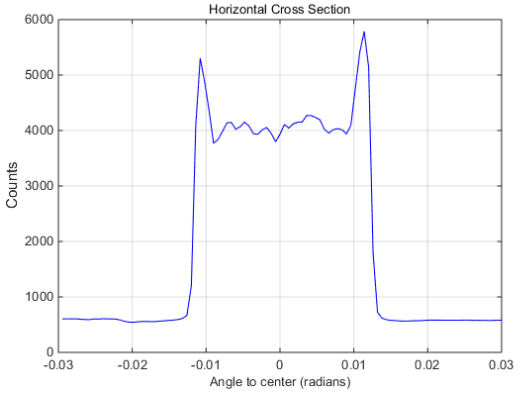

(d) Horizontal cross section of corrected image.

Fig. 5.5: Corrected images from ambient output beam uniformity test.

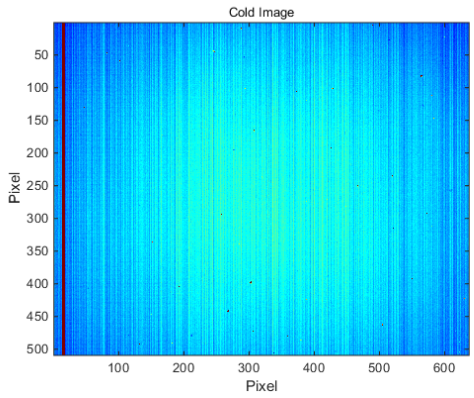

(a) Image of ambient temperature blackbody.

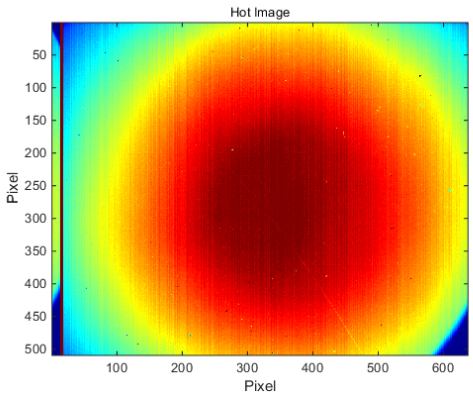

(b) Image of 100°C blackbody.

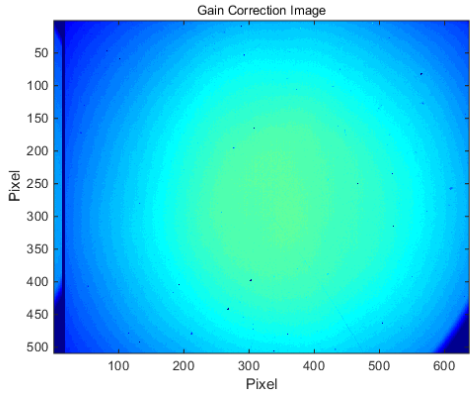

(c) Gain correction image.

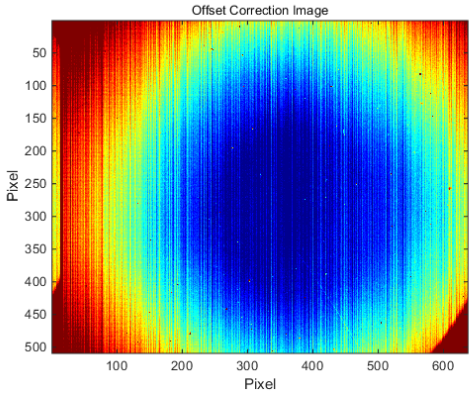

(d) Offset correction image.

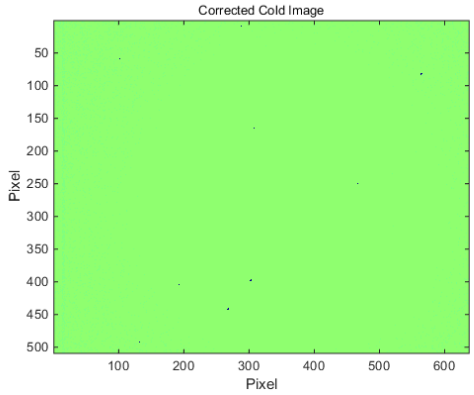

(e) Corrected ambient blackbody image after offset and gain correction.

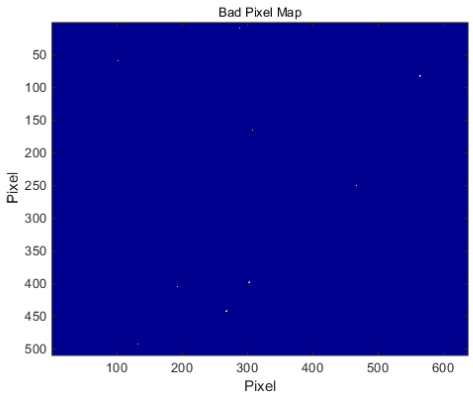

(f) Bad pixel map.

Fig. 5.6: Example of correction images used to correct the output uniformity data from the thermal vacuum tests.

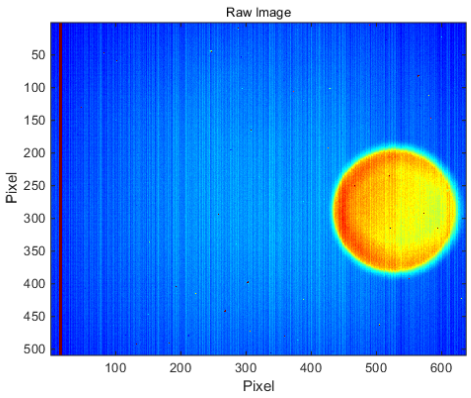

(a) Raw image of QCL source system output beam.

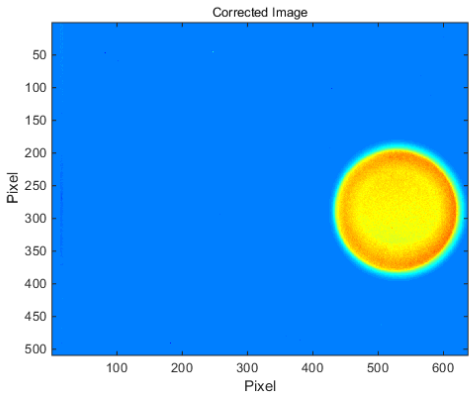

(b) Corrected image of QCL source system output beam.

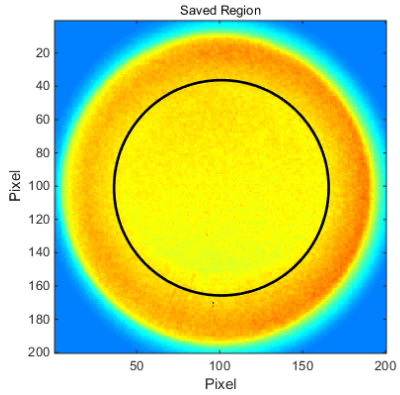

(c) Frame centered on beam with outer edge pixels removed. 10-mm diameter region on interest marked by black circle.

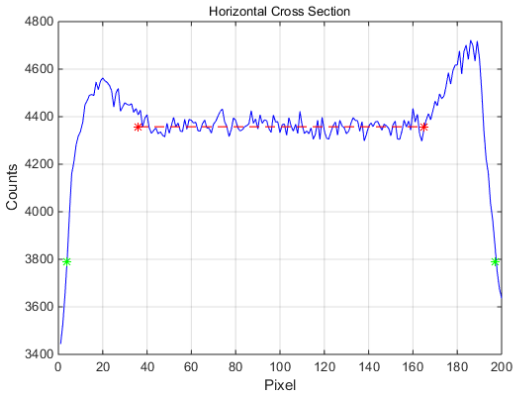

(d) Horizontal cross section of corrected image.

Fig. 5.7: Corrected images from ambient output beam uniformity test.

After the data was in the format explained above, the central region of interest in the output beam was fit to a 37-term Zernike polynomial. This was done in order to characterize the optical artifacts in the data due to large scale structure. The Zernike fit was subtracted from the data leaving a residual signal consisting of speckle, specularly reflected beamlets, and other random noise components. Figure 5.8 shows an example of the Zernike fit to a set of data from the ambient output uniformity test. Fig. 5.8a shows an image of the data before the Zernike fit was applied, Fig. 5.8b shows an image of the data after the Zernike fit was applied, Fig. 5.8c shows an image of the residual data after the Zernike fit was subtracted from the original corrected image, and Fig. 5.8d shows a three-dimensional plot

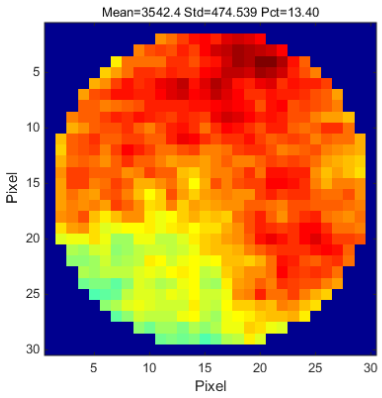

(a) Image data before Zernike fit.

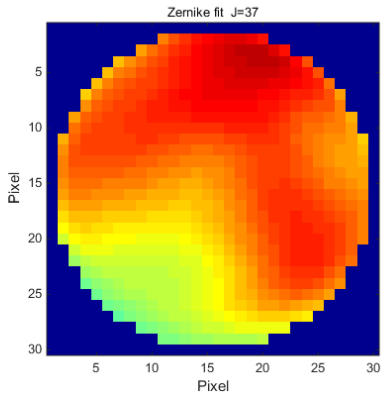

(b) Image data after Zernike fit.

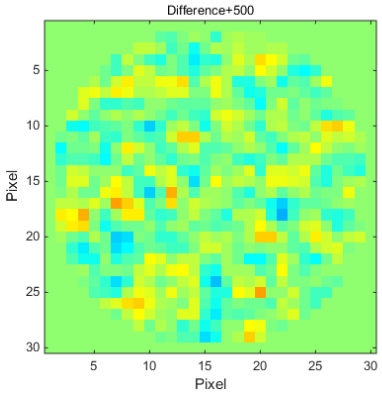

(c) Residual signal after subtracting the Zernike fit from the data.

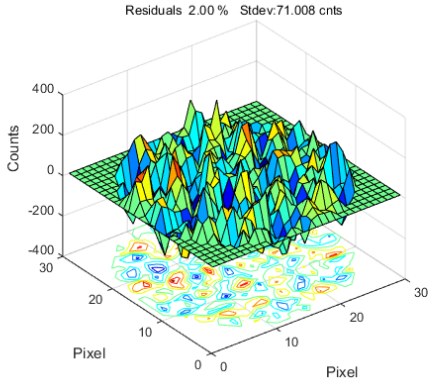

(d) Three dimensional plot of the residuals displaying the standard deviation from zero mean.

Fig. 5.8: Zernike fit to ambient output beam uniformity data.

of the residuals with zero mean. Five-hundred counts were added to Fig. 5.8c so that it is possible to discern between the positive and negative counts.

5.2.4 Radiance Calibration Test

The goal of the radiance calibration test was to ascertain the absolute radiance of the output beam from the source system. Similar to the stability test data, the first process performed on the radiance test data was to remove the background noise measured by the power meter. This was accomplished in the same manner explained in the stability test. To calculate the absolute radiance of the output beam from the system, the responsivity of the power meter needed to be calculated. This calculation was performed using the

geometry of the hardware configuration from the blackbody measurements. This hardware configuration is shown in Fig. 5.9 for the ambient test.

The aperture in the hardware configuration of Fig. 5.9 was 25.4 mm away from the blackbody. The blackbody was at a temperature of 701.5 C. The radiance from the blackbody caused the aperture to heat up to a point where the aperture effectively became a second blackbody whose radiance was also measured by the power meter. Due to this issue with the experimental setup the absolute radiance values calculated from the ambient test data are inaccurate. This hardware configuration error was realized before the data was collected for the thermal vacuum tests, and the configuration of the blackbody measurement was improved. The first improvement to the hardware configuration was the addition of a second aperture that was positioned closer to the power meter, which reduces the radiant flux received by the power meter from the aperture close to the blackbody. The second improvement to the hardware configuration was that the aperture closest to the blackbody was moved farther away from it so it would not get as hot. Figure 5.10 shows the hardware configuration of the blackbody measurement for the thermal vacuum test. Equations (5.2)–(5.7) are derived from Figures 5.9 and 5.10, where the equation parameters are defined in Table 5.1.

$$\theta_{PM_{BB}} = tan^{-1}\frac{d_{PM}}{2l_{PM_{BB}}} \tag{5.2}$$

$$A_{BB} = \pi\left(\frac{d_{BB}}{2}\right)^2 \tag{5.3}$$

$$\Omega_{PM_{BB}} = \pi sin^2\theta_{PM_{BB}} \tag{5.4}$$

$$L_{BB}(\Delta\lambda, T) = \int_{\lambda_1}^{\lambda_2} \frac{2hc^2}{\lambda^5}\frac{1}{e^{\frac{hc}{\lambda k_B T}} - 1}d\lambda \tag{5.5}$$

$$\Phi_{REC_{BB}} = L_{BB}(\Delta\lambda, T)A_{BB}\Omega_{PM_{BB}}\tau_{SF}\tau_{CaF_2} \tag{5.6}$$

$$R_\Phi = \frac{P_{PM_{BB}}}{\Phi_{REC_{BB}}} \tag{5.7}$$

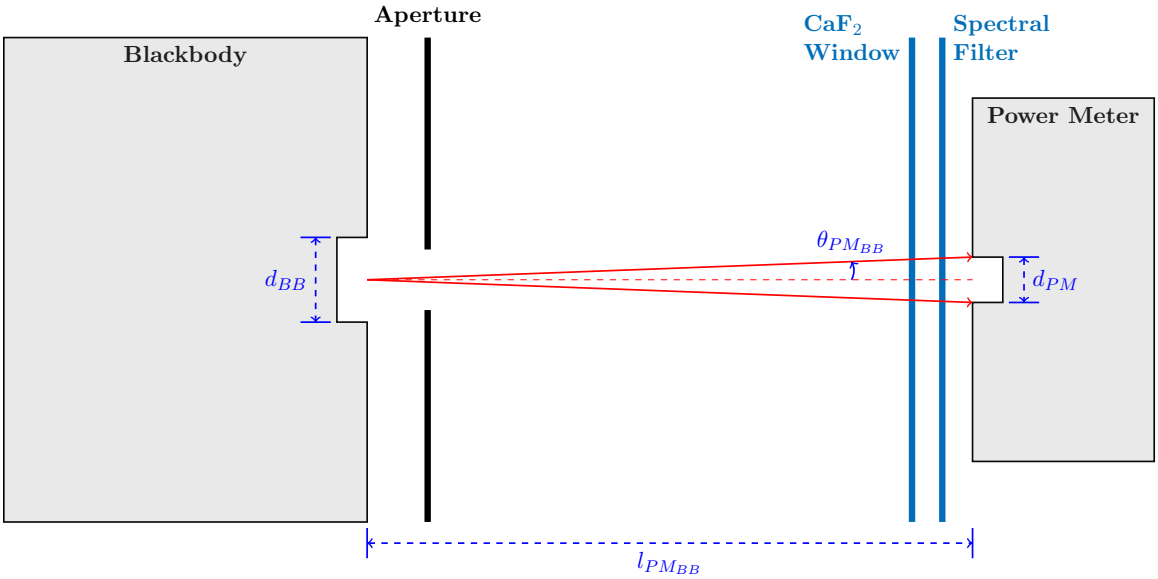

Fig. 5.9: Geometry of ambient test hardware configuration for blackbody power measurements.

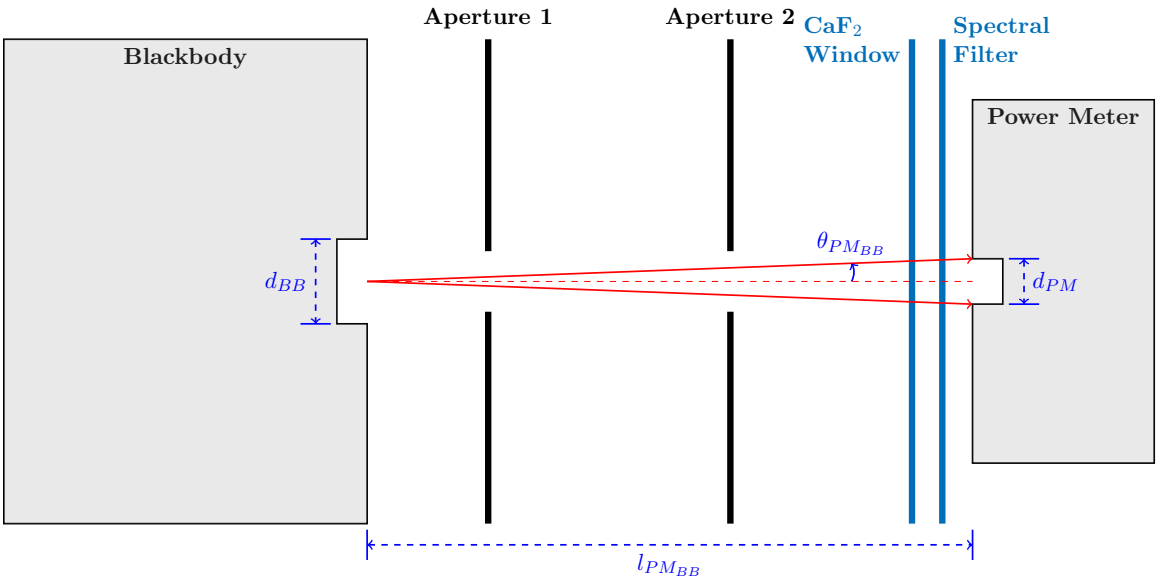

Fig. 5.10: Geometry of ambient test hardware configuration for blackbody power measurements.

Once the responsivity of the power meter was known the radiance of the QCL source system was calculated using the geometry in Fig. 5.11, and Equations (5.8)–(5.12), where the equation parameters are defined in Table 5.2. Figure 5.12 shows the average radiance of the QCL source system for both the ambient and thermal vacuum tests. The issue of the

Table 5.1: Parameter definitions for Equations (5.2)–(5.7)

Parameter	**Definition**
d_{BB}	Blackbody Aperture Diameter
d_{PM}	Power Meter Sensor Diameter
$l_{PM_{BB}}$	Distance from Blackbody to Power Meter
$\theta_{PM_{BB}}$	Power Meter FOV
A_{BB}	Blackbody Aperture Area
$\Omega_{PM_{BB}}$	Solid Angle Incident on Power Meter from Blackbody
$L_{BB}(\Delta\lambda, T)$	Radiance from Blackbody (Planck's Equation)
$\Phi_{REC_{BB}}$	Flux Received from Blackbody
τ_{SF}	Transmittance of the Spectral Filter
τ_{CaF_2}	Transmittance of the Calcium Fluoride Window
$P_{PM_{BB}}$	Power Measured by Power Meter from Blackbody
R_{Φ}	Responsivity of Power Meter

radiance from the blackbody causing the aperture closest to it to heat up was not entirely resolved in the thermal vacuum experiment configuration. Because of this, the calculated values for the absolute radiance contain some error. No estimate of the magnitude of the error is available because the temperature of the aperture was not measured in any of the tests. However, the values for the absolute radiance calculated from the thermal vacuum test data are more accurate than the values calculated from the ambient test data due to the improvements made to the hardware configuration between those two tests.

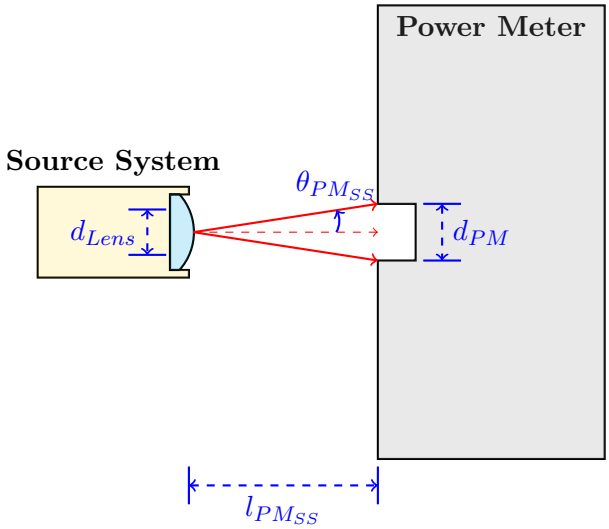

Fig. 5.11: Geometry of hardware configuration from QCL source system power measurement.

$$\theta_{PM_{SS}} = tan^{-1}\frac{d_{PM}}{2l_{PM_{SS}}} \tag{5.8}$$

$$A_{Lens} = \pi\left(\frac{d_{Lens}}{2}\right)^2 \tag{5.9}$$

$$\Omega_{PM_{SS}} = \pi sin^2\theta_{PM_{SS}} \tag{5.10}$$

$$\Phi_{REC_{SS}} = \frac{P_{PM_{SS}}}{R_\Phi} = L_{SS}A_{Lens}\Omega_{PM_{SS}} \tag{5.11}$$

$$L_{SS} = \frac{\Phi_{REC_{SS}}}{A_{Lens}\Omega_{PM_{SS}}} \tag{5.12}$$

Table 5.2: Parameter definitions for Equations (5.8)–(5.12)

Parameter	**Definition**
d_{Lens}	Output Lens Aperture Diameter
d_{PM}	Power Meter Sensor Diameter
$l_{PM_{SS}}$	Distance from QCL Source System to Power Meter
$\theta_{PM_{SS}}$	Power Meter FOV
A_{Lens}	Output Lens Aperture Area
$\Omega_{PM_{SS}}$	Solid Angle Incident on Power Meter from QCL Source System
$P_{PM_{SS}}$	Power Measured by Power Meter from QCL Source System
$\Phi_{REC_{SS}}$	Flux Received from QCL Source System
R_{Φ}	Responsivity of Power Meter
L_{SS}	Radiance from QCL Source System

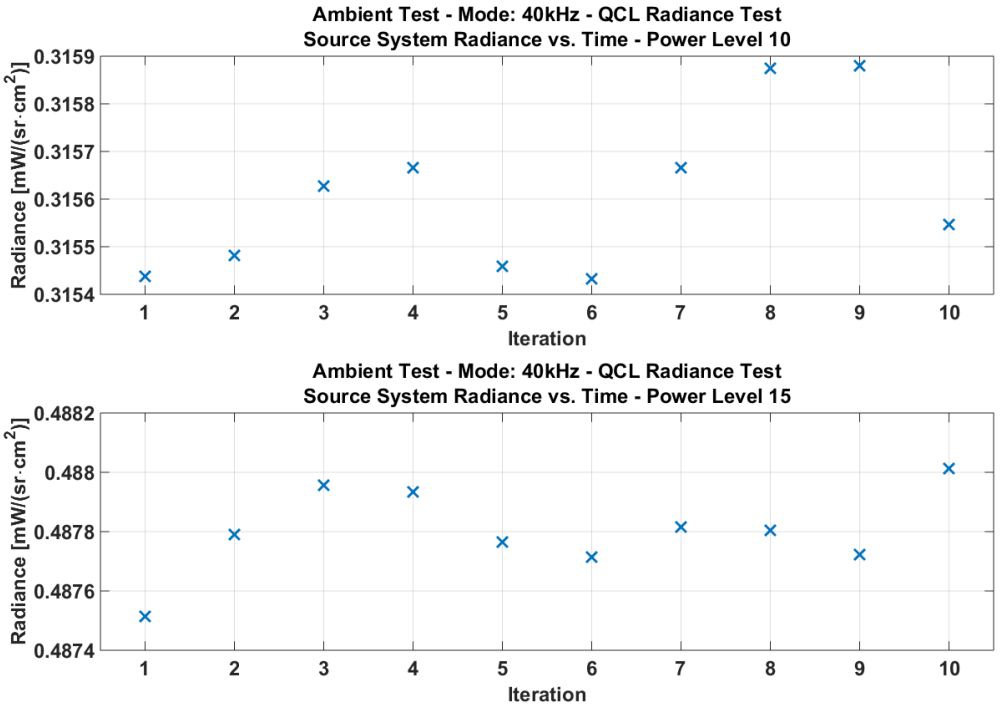

(a) Radiance of QCL source system in ambient test.

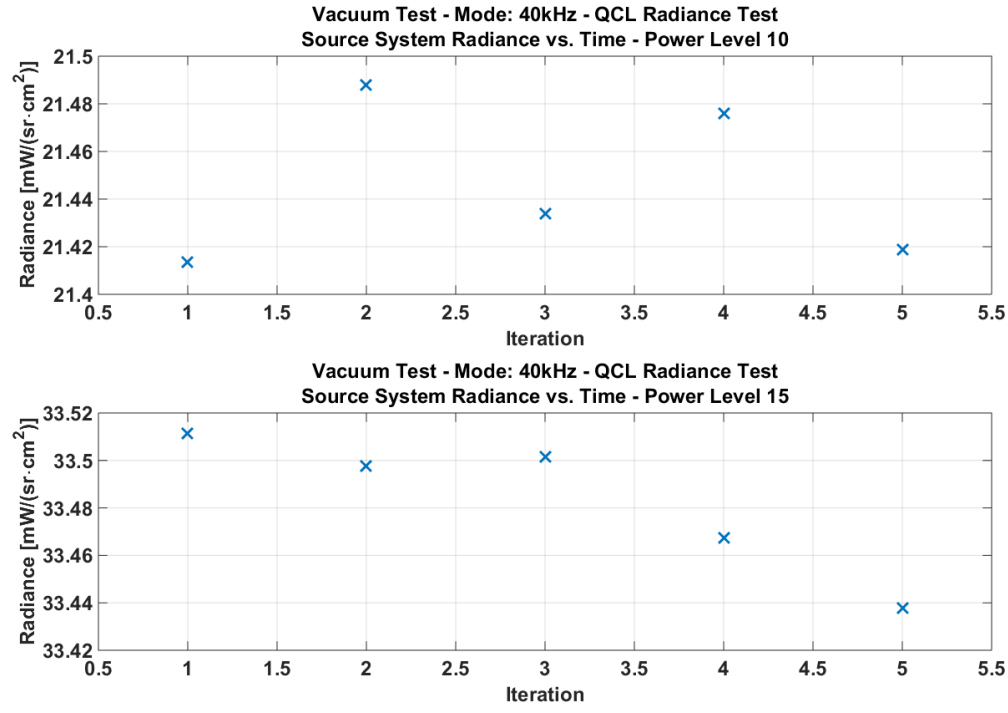

(b) Radiance of QCL source system in vacuum test.

Fig. 5.12: Radiance of QCL source system.

Chapter 6

Comparison of Simulation Results and Actual Test Data

To compare the simulation results with the actual measured data, a special simulation environment was created. In this environment, the irradiance and intensity detectors were modified to have the same number of pixels as the IR camera being used for the actual measurements. To get a good set of simulation data, eight-hundred million rays were traced through the optical system. Figure 6.1 shows the irradiance and intensity measured at the output of the lens in the simulation.

It was desired to compare the region of interest in each of the images, so the 10-mm central diameter of the irradiance plot, and the 5° radius of the intensity plot were extracted from the simulation data. An average and standard deviation was calculated over all of the pixels in the region of interest for a quantitative comparison. Figures 6.2 and 6.3 show the ray trace simulation data for the regions of interest.

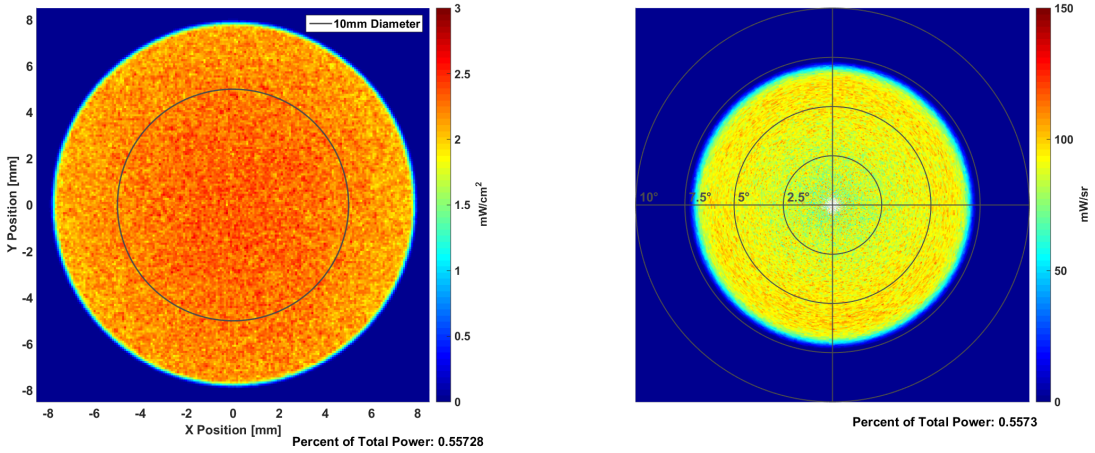

(a) Simulated output irradiance from the QCL source system.

(b) Simulated output intensity from the QCL source system.

Fig. 6.1: Simulated irradiance and intensity plots of the final optical model for comparison with actual measured data.

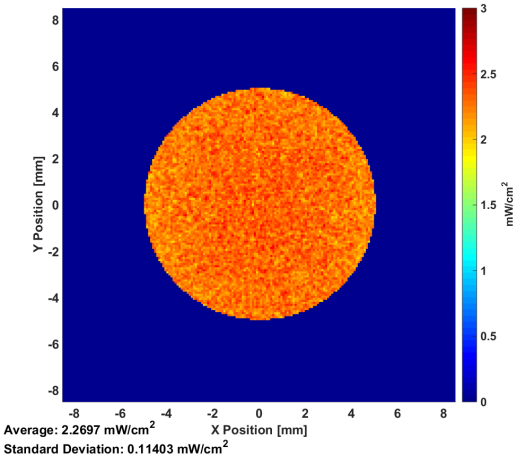

(a) 10-mm region of interest of simulated QCL source system irradiance.

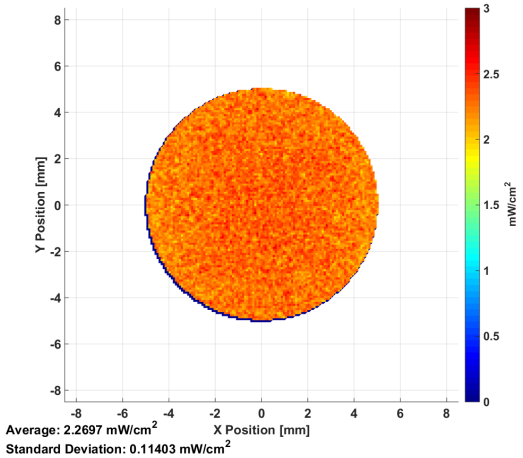

(b) 10-mm region of interest of simulated QCL source system irradiance with background removed.

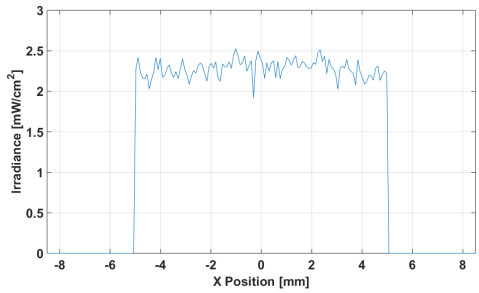

(c) 10-mm region of interest of simulated QCL source system irradiance X cross section.

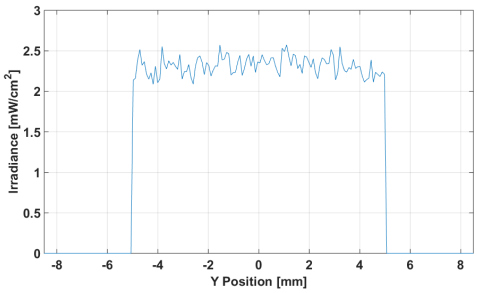

(d) 10-mm region of interest of simulated QCL source system irradiance Y cross section.

Fig. 6.2: Simulated QCL source system output irradiance.

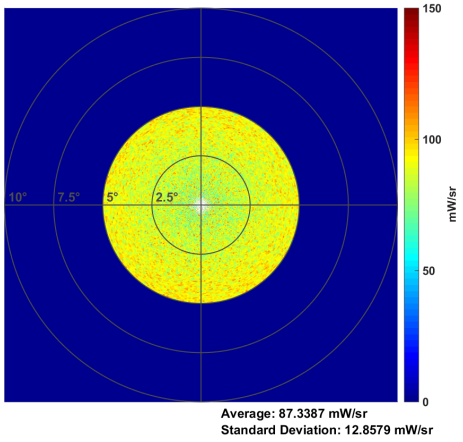

(a) 5° radius of interest of simulated QCL source system intensity.

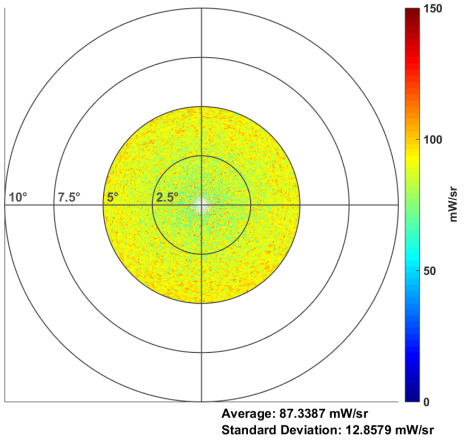

(b) 5° radius of interest of simulated QCL source system intensity with background removed.

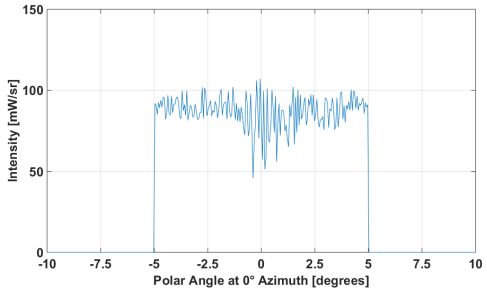

(c) 5° radius of interest of simulated QCL source system intensity 0° azimuth cross section.

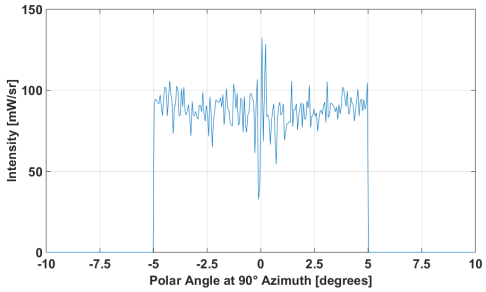

(d) 5° radius of interest of simulated QCL source system intensity 90° azimuth cross section.

Fig. 6.3: Simulated QCL source system output intensity.

The simulation results provide irradiance data in units of $\frac{mW}{cm^2}$ and intensity data in units of $\frac{mW}{sr}$. The actual measured data is in terms of relative counts of photons that hit the pixels on the detector. In order to compare these two sets of results, a percent deviation was calculated by dividing the standard deviation by the mean, and multiplying by one-hundred. This percent deviation can be compared directly between the two sets of data, because it is a unitless parameter that represents change in the uniformity of the output beam. Table 6.1 gives a comparison of the percent deviation that was calculated using the data from the simulations results, ambient tests, and vacuum tests. From these results, it is clear that the angular uniformity of the output beam is better than the simulated model, and the spatial uniformity of the beam is just about as good as in the simulated model.

Table 6.1: Output uniformity test comparison to simulation results.

	Simulation		**Ambient Test**		**Vacuum Test**	
	Anglular	**Spatial**	**Anglular**	**Spatial**	**Anglular**	**Spatial**
% Deviation $(100 * \frac{\sigma}{\mu})$	14.72	5.02	7.28	6.65	3.87	5.56

Chapter 7

Conclusion

The research presented in this thesis describes the design of an optical system that enables the use of QCLs as in-flight calibration sources in space-based remote sensing systems. The optical system transforms the output beam from a QCL so that it is both spatially and angularly uniform at the desired beam diameter and divergence. An optical model for the design was simulated to verify that the optical system would create a uniform beam that could be used for calibration. The optical system was implemented in hardware and characterized. The characterization showed that the physical realization of the system does generate an output beam that can be used for in-flight instrument calibration in space-based remote sensing systems.

Future work in this research area would involve identifying specific missions that would benefit from having a QCL-based calibration source system on board the spacecraft, and integrating such a system into the payload design for those missions. A design similar to that presented in this thesis could then be used as a baseline for the in-flight calibration source system.

References

[1] J. Tansock, S. Hansen, K. Paskett, A. Shumway, J. Peterson, J. Stauder, L. Gordley, Y. Wang, M. Melbert, J. Russell Iii *et al.*, "Saber ground calibration," *International Journal of Remote Sensing*, vol. 24, no. 2, pp. 403–420, 2003.

[2] J. Faist, F. Capasso, D. L. Sivco, C. Sirtori, A. L. Hutchinson, and A. Y. Cho, "Quantum cascade laser," *Science*, vol. 264, no. 5158, pp. 553–556, 1994.

[3] J. Faist, *Quantum Cascade Lasers*. Oxford University Press, 2013.

[4] D. A. Neamen, *Semiconductor Physics and Devices*, 4th ed. McGraw-Hill, 2012.

[5] Y. Yao, A. J. Hoffman, and C. F. Gmachl, "Mid-infrared quantum cascade lasers," *Nature Photonics*, vol. 6, no. 7, pp. 432–439, 2012.

[6] R. Maulini, "Broadly tunable mid-infrared quantum cascade lasers for spectroscopic applications," Ph.D. dissertation, Scuola Normale Superiore, Pisa, 2006.

[7] *4550 nm Quantum Cascade Laser, 450mW*, Thorlabs, October 2014, rev D.

[8] S. M. Hansen, "Precision current control for quantum cascade lasers as flight calibration sources," Master's thesis, Utah State University, 2014.

[9] B. G. Crowther, K. J. Thome, S. F. Biggar, and C. J. Burkhart, "Internally baffled integrating sphere cosine collector," in *Optical Science, Engineering and Instrumentation'97*. International Society for Optics and Photonics, 1997, pp. 246–252.

[10] R. W. Boyd, *Radiometry and the detection of optical radiation*. John Wiley and Sons, New York, NY, USA, 1983.

[11] *Technical Guide: Reflectance Materials and Coatings*, Labsphere, North Sutton, NH.

[12] W. Welford and R. Winston, *High Collection Nonimaging Optics*. Academic Press, 1989.

[13] F. E. Nicodemus, J. C. Richmond, J. J. Hsia, I. W. Ginsberg, and T. Limperis, *Geometrical considerations and nomenclature for reflectance*. US Department of Commerce, National Bureau of Standards Washington, DC, USA, 1977, vol. 160.

[14] B. Balling, "A comparative study of the bidirectional reflectance distribution function of several surfaces as a mid-wave infrared diffuse reflectance standard," AIR FORCE INST OF TECH WRIGHT-PATTERSON AFB OH GRADUATE SCHOOL OF ENGINEERING AND MANAGEMENT, Tech. Rep. No. AFIT/GE/ENP/09-M01, 2009.

[15] T. L. Myers, B. D. Cannon, M. S. Taubman, and B. E. Bernacki, "Performance and reliability of quantum cascade lasers," in *SPIE Defense, Security, and Sensing*. International Society for Optics and Photonics, 2013, pp. 87 330E–87 330E.

[16] M. Planck, *The theory of heat radiation*, 2nd ed. P. Blakistonś Son & Co., 1914, ch. 4, p. 168.